Evaluation of nonlocal and local planetary boundary layer schemes in the WRF model

Bo Xie,[1] Jimmy C. H. Fung,[1,2] Allen Chan,[1] and Alexis Lau[1,3]

[1]   A realistic reproduction of planetary boundary layer (PBL) structure and its evolution is critical to numerical simulation of regional meteorology and air quality. Conversely, insufficient realism in the simulated physical properties often leads to degraded meteorological and air quality prognostic skills. This study employed the Weather Research and Forecasting model (WRF) to evaluate model performance and to quantify meteorological prediction differences produced by four widely used PBL schemes. Evaluated were two nonlocal PBL schemes, YSU and ACM2, and two local PBL schemes, MYJ and Boulac. The model grid comprised four nested domains at horizontal resolutions of 27 km, 9 km, 3 km and 1 km respectively. Simulated surface variables 2 m temperature and 10 m wind at 1 km resolution were compared to measurements collected in Hong Kong. A detailed analysis of land-atmosphere energy balance explicates heat flux and temperature variability among the PBL schemes. Differences in vertical profiles of horizontal velocity, potential temperature, bulk Richardson number and water vapor mixing ratio were examined. Diagnosed PBL heights, estimated by scheme specific formulations, exhibited the large intrascheme variance. To eliminate formulation dependence in PBL height estimation, lidar measurements and a unified diagnosis were jointly used to reanalyze PBL heights. The diagnosis showed that local PBL schemes produced shallower PBL heights than those of nonlocal PBL schemes. It is reasonable to infer that WRF, coupled with the ACM2 PBL physics option can be a viable producer of meteorological forcing to regional air quality modeling in the Pearl River Delta (PRD) Region.

1.   Introduction

[2]   The WRF model is widely used for meteorological research application and forecasting. With the fast development in computer power, numerical models are able to operate with unprecedented grid resolutions. Nonetheless, many of the important physical processes in the atmosphere cannot be completely resolved by the current resolutions and must be parameterized. These processes include the microphysics of cloud formation and precipitation; the transfer of heat, moisture, and momentum at the air–surface interface, and the heat exchange associated with atmospheric radiation. Among the processes, the formation, structure,

and maintenance of the planetary boundary layer is critical to the prediction of meteorological properties and airborne chemical components. Turbulence is a dominant factor in atmospheric stability throughout the PBL by means of turbulent mixing of heat, momentum and moisture. The aggregate impact of turbulent motions on grid-scale variables is expressed through PBL parameterizations in meteorological models. Obviously a realistically modeled PBL structure is crucial to not only numerical weather prediction and research, but also to air quality studies and other environmental investigations.

[3]   During the past 40 years, considerable progress has been made in the development and improvement of the PBL parameterizations [e.g., *Mellor and Yamada*, 1974, 1982; *Blackadar*, 1976, 1979; *Zhang and Anthes*, 1982; *Burk and Thompson*, 1989; *Bougeault and Lacarrére*, 1989; *Janjić*, 1994; *Hong and Pan*, 1996; *Hong et al.*, 2006; *Pleim*, 2007a, 2007b] in atmospheric models. In WRF, PBL processes can be parameterized either through local closure schemes (e.g., K-theory in *Stull* [1988]) or through nonlocal closure schemes. The former method is best suited for shear turbulence in stable conditions. However, mixing in the convective boundary layer (CBL) is achieved by sub-grid scale eddies and large asymmetrical thermals. K-theory is limited to simulating turbulent mixing within adjacent layers

[1]Division of Environment, Hong Kong University of Science and Technology, Hong Kong.
[2]Department of Mathematics, Hong Kong University of Science and Technology, Hong Kong.
[3]Department of Civil and Environmental Engineering, Hong Kong University of Science and Technology, Hong Kong.

Corresponding author: J. C. H. Fung, Division of Environment, Hong Kong University of Science and Technology, Clear Water Bay, Kowloon, Hong Kong. (majfung@ust.hk)

symmetrically, thus the mixing is not appropriately reproduced. Various nonlocal closure models have been developed to overcome the shortcomings of K-theory in producing turbulent mixing in the PBL. The nonlocal upward transport by buoyant plumes can be included as a parameterized adjustment term which represents large-scale motions [*Holtslag and Boville*, 1993; *Hong and Pan*, 1996; *Hong et al.*, 2006], such as in the Medium Range Forecast (MRF) PBL scheme. Or it can be simulated by explicitly treating the upward and downward transport of conserved atmospheric scalars [*Stull*, 1984; *Blackadar*, 1979; *Pleim and Chang*, 1992; *Pleim*, 2007a], such as in the Asymmetric Convective Model version 1 (ACM1) PBL scheme. *Hong et al.* [2006] revised the vertical diffusion package in the MRF PBL scheme and renamed it as the Yonsei University (YSU) PBL scheme, which explicitly treats entrainment processes. The YSU PBL scheme is found to increase boundary layer mixing in the thermally induced free convection regime and to reduce it in the mechanically induced forced convection regime, which yields a more realistic PBL structure than that predicted in MRF. *Pleim* [2007a] adds a local eddy diffusion component to the ACM1 algorithm [*Pleim and Chang*, 1992] and demonstrates that it can better represent the shape of vertical profiles by taking into account both the sub-grid and super-grid components of turbulence transport in the CBL. Further, the explicit treatment of nonlocal fluxes in Asymmetric Convective Model version 2 (ACM2) is expected to properly simulate a wider array of quantities in addition to heat. A recent update to the YSU [*Hong*, 2010] and ACM2 PBL schemes signify important enhancements to the available WRF physics options. The performance of these schemes will be evaluated in this paper.

1.1. Overview of Impact of PBL Schemes on Meteorological and Air Quality Modeling

[4] A number of studies have examined the sensitivity of meteorological models such as MM5 and WRF predictions to the choice of PBL schemes. *Zhang and Zheng* [2004] conducted a 3-day MM5 simulation with a resolution of 36 km in summertime over the central United States to evaluate the performances of five PBL parameterizations. They concluded that nonlocal Blackadar PBL scheme performs best among the five PBL schemes in reproducing the diurnal cycles of surface wind, mainly because this nonlocal scheme allows direct mass and momentum exchanges between the surface layer and the layers above in the unstable PBL. Moreover, its nocturnal module is resolved with three different stability regimes based on the bulk Richardson number. *Berg and Zhong* [2005] found that nonlocal PBL schemes produced more well-mixed daytime boundary layers than those produced by the local PBL scheme. This was discovered by running MM5 at a high resolution of 500 m. The mixed layer depths are generally well estimated by the nonlocal Blackadar scheme but underestimated by the local scheme. *Hu et al.* [2010] conducted WRF simulations spanning three summer months with three PBL schemes (MYJ, YSU and ACM2) and compared them with surface and boundary layer observations in the south-central United States. It is concluded that MYJ PBL scheme has weaker entrainment processes at the top of PBL due to weaker vertical mixing, thus resulting in lower temperature and higher moisture near the surface than other two PBL schemes. They

primarily attribute MYJ's weak vertical mixing to no consideration of penetrating plumes or large eddies in this local PBL scheme.

[5] Meteorological conditions are known to exert direct impact on the air quality simulation [*Seaman*, 2000]. *Han et al.* [2008] discovered that the difference in modeled vertical turbulent mixing is one of the main reasons for the discrepancy in pollutant concentration among the chemical transport models. Hence, it is of particular value to understand the similarities and discrepancies between the PBL schemes' prediction skills and the ensuing impact on air quality modeling. Where the physical effects of land surface elements are significant, such as in highly urbanized areas, understanding the ability of nonlocal schemes to blend turbulent mixing characteristics near and far away from the surface can be a crucial factor in simulating regional transport and dispersion.

1.2. Objectives

[6] Contrary to previous studies that emphasized middle-latitude continental regions of mild topographic variability, this study focuses on a geographically complex subtropical domain that centers in Hong Kong, and extends to Greater Pearl River Delta (PRD) region. The PRD region comprises multiple megacities that experience rapid ongoing economic expansion, which brings it tremendous release of air pollutants and considerable deterioration of natural and human resources. The study aims to quantify the sensitivity of key WRF meteorological predictions to four often used PBL schemes. Model results at 1 km grid resolution are compared with each other and with an extensive data set of surface measurements over Hong Kong territories. This study contributes a novel and rigorous evaluation of WRF performance and of its sensitivity to PBL parameterizations in 1 km-by-1 km grid resolution over Hong Kong. It is informative and valuable to understand the atmospheric turbulence, air-surface exchange processes and the uncertainties of these schemes on predictions for air quality modeling and assessment. Although considerable efforts have been made to focus on the comparison between predictions by various PBL schemes and measurements, few studies have attempted to relate the root causes of modeled differences to the different assumptions or parameterizations in each scheme. Neither have previous studies elucidated the model processes nor the typical characteristics of one PBL scheme compared to others. This study aims to address these issues: (1) What differences exist among key WRF predicted meteorological variables resulting from the choice of PBL schemes? (2) Is there a preferred WRF PBL scheme for the Hong Kong region?

[7] Section 2 provides descriptions of model setup and configurations including key components and domain definition in this study. Section 3 briefly describes the four PBL schemes. Section 4 presents experimental design and WRF results for the evaluation of surface and vertical meteorological variables. Summary and concluding remarks follow in the final section.

2. Model Setup and Configurations

2.1. Domain Settings

[8] Four nested domains with horizontal grid resolutions of 27 km, 9 km, 3 km, and 1 km are used. Figure 1 shows the
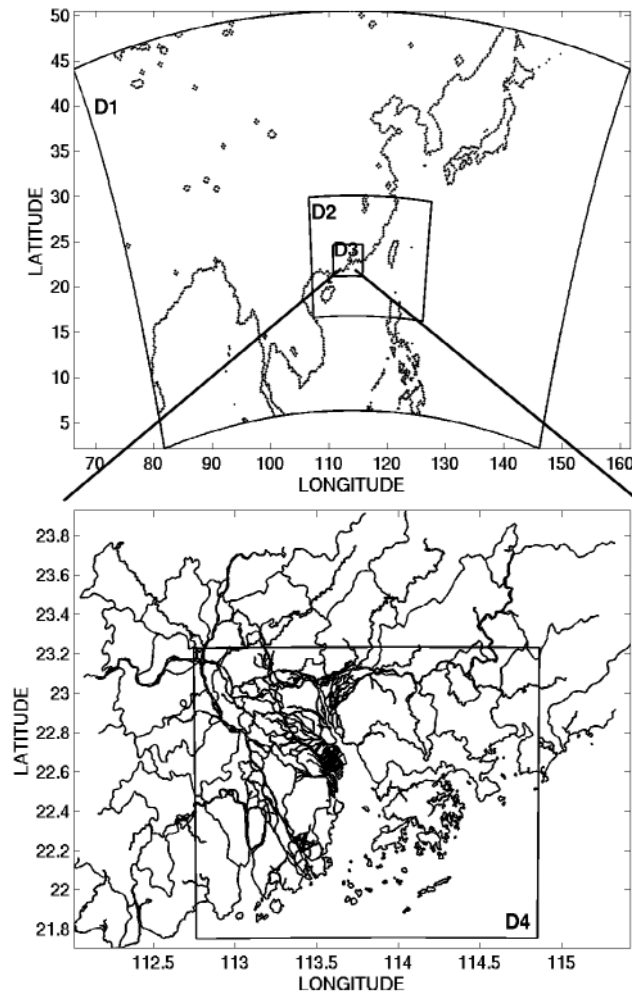
Figure 1. The nested WRF domains (black line) at horizontal spacing of 27 km (Domain 1), 9 km (Domain 2), 3 km (Domain 3) and 1 km (Domain 4).

geographic coverage of the four domains. Specifically, Domain 1 covers central/eastern China and the South China Sea; Domain 2 covers South China; Domain 3 covers the Pearl River Delta, and Domain 4 covers the Hong Kong territory. Lambert-Conformal map projection is used with the projection parameters set to $\alpha = 15°$, $\beta = 40°$, $\gamma = 114°$, center longitude = 114°E and center latitude = 28.5°N.

[9] The WRF terrain following coordinate contains 39 sigma levels. The lowest sigma levels of model are 0.9979, 0.9956, 0.9931, 0.9904, and 0.9875. The corresponding heights are around 18 m, 37 m, 57 m, 80 m and 104 m above ground level (AGL). The layer thickness of the layers increases gradually with height. The model top pressure is set to 50 hPa, about 20 km AGL. To resolve in detail the complicated processes near the surface, 21 sigma levels are assigned to occupy the lowest 2 km AGL in the PBL.

2.2. Configurations of WRF

[10] The lateral boundary conditions for the coarsest domain and analyses used in four dimensional data assimilation (FDDA) were obtained from NCEP FNL (Final) Operational Global Analysis data with a horizontal resolution of 1° in latitude and longitude, and a temporal resolution of six-hour. Initial condition was generated with the same global analysis data, but refined with NCEP ADP Operational Global Upper Air and Surface Observations via objective analysis. FDDA has been shown to improve the accuracy of the meteorological simulation [*Stauffer and Seaman*, 1990, 1994]. *Stauffer and Seaman* [1994] discovered that performing analysis nudging on the mesoscale coupled with observational nudging on the finest scale gives rise to the best outcome. Therefore, analysis nudging is applied in Domain 1 for wind, temperature and moisture. Wind and moisture are nudged in all vertical layers. Temperature is nudged above the PBL. Wind data measured at 10 m AGL in Hong Kong is used for observation nudging at surface in Domain 4 only in this study. The Rapid Radiative Transfer Model (RRTM) longwave radiation scheme, the Dudhia shortwave radiation scheme, the WRF Single-Moment 3-class microphysics scheme and the Noah Land Surface Model are applied in all domains. The Grell-Devenyi ensemble cumulus scheme is applied in Domain 1 and Domain 2. Two-way nesting is applied [*Skamarock et al.*, 2008].

3. Brief Descriptions of PBL Schemes and Surface Layer Schemes

[11] Four PBL schemes are investigated in this study, including two first-order closure schemes – the Yonsei University (YSU) PBL [*Hong et al.*, 2006] and Asymmetric Convective Model version 2 (ACM2) PBL [*Pleim*, 2007a, 2007b], and two turbulent kinetic energy (TKE) closure schemes – the Mellor-Yamada-Janjić (MYJ) PBL [*Janjić*, 1990, 1996, 2002] and Bougeault – Lacarrere (Boulac) PBL [*Bougeault and Lacarrére*, 1989].

3.1. YSU PBL Scheme

[12] YSU is characterized as a nonlocal closure scheme. For the mixed layer, following the "nonlocal K" approach and further reformulation [*Troen and Mahrt*, 1986; *Holtslag and Boville*, 1993; *Hong and Pan*, 1996; *Noh et al.*, 2003], YSU adds a nonlocal gradient adjustment term γ_c to express the turbulent diffusion:

$$\frac{\partial C}{\partial t} = \frac{\partial}{\partial z}\left[K_c \left(\frac{\partial C}{\partial z} - \gamma_c \right) - \overline{(w'c')}_h \left(\frac{z}{h}\right)^3 \right] \quad (1)$$

where C represents heat or momentum variable, K_c is the eddy diffusivity coefficient, γ_c is a correction to the local gradient, which incorporates the contribution of the large-scale eddies to the total flux, and $\overline{(w'c')}_h$ is the flux at the inversion layer. It should be noted that the countergradient mixing term γ_c is not applied to passive variables (e.g., water vapor q) in the YSU since these variables are not necessarily correlated with the thermals. One critical revision in YSU vertical diffusion package is to include an asymptotic entrainment flux term at the inversion layer $-\overline{(w'c')}_h \left(\frac{z}{h}\right)^3$, through which treatments of the entrainment process become explicit [*Hong et al.*, 2006].

3.2. ACM2 PBL Scheme

[13] ACM2 is a combination of the ACM1 and local eddy diffusion, or in other words a combination of nonlocal and local closure. Unlike YSU using a parameterized adjustment term, ACM2 treats nonlocal fluxes using a transilient matrix. Because of this explicit definition for nonlocal fluxes, ACM2 is intended to be more applicable to other quantities such as humidity, winds, or trace chemical mixing ratios in addition to heat components. Below is the ACM2 governing equation for any scalar C_i

$$\frac{\partial C_i}{\partial t} = f_{conv} Mu C_1 - f_{conv} Md_i C_i + f_{conv} Md_{i+1} C_{i+1} \frac{\Delta z_{i+1}}{\Delta z_i}$$
$$+ \frac{\partial}{\partial z} \left[K_c (1 - f_{conv}) \frac{\partial C_i}{\partial z} \right] \qquad (2)$$

where Mu is the nonlocal upward convective mixing rate, Md_i is the downward mixing rate from layer from layer i to layer $i - 1$, C_1 represents the scalar at the lowest model layer and Δz_i is the thickness of layer i. f_{conv} is the key parameter to control the contribution of nonlocal mixing versus that of local mixing. This partitioning factor f_{conv} is derived from the ratio of nonlocal heat flux to total heat flux at the top of the surface layer ($0.1\ h$) according to the model described by *Holtslag and Boville* [1993]. As a result, f_{conv} behaves as a simple function of stability (h/L) where it ramps up quickly from zero for stable or neutral conditions with increasing instability then leveling off at around 0.5 for very unstable conditions. f_{conv} is defined as,

$$f_{conv} = \left[1 + \frac{k^{-2/3}}{0.1a} \left(-\frac{h}{L} \right)^{-1/3} \right]^{-1} \qquad (3)$$

where a is a constant set to 7.2, k is the von Karman constant whose value is 0.4, h is the PBL height and L is the Monin-Obukhov length scale.

[14] On the right hand side of equation 2, the first term represents nonlocal upward fluxes from the surface. The second term indicates compensating downward fluxes to the adjacent lower layer. The third term signifies the asymmetric downward fluxes from the adjacent upper layer. The last term represents the local upward eddy diffusion [*Pleim*, 2007a, 2007b].

[15] The nonlocal mass exchange in ACM2 PBL is a physical representation of upward transport by detraining convective plumes that applies to any quantity. Other models apply an adjustment term to represent the large scale convection (nonlocal behavior) driven by surface heat flux, which is most valid for heat since surface heat flux is both the source and driver of the convective turbulence. However, for other quantities such as chemical emission, the assumption in those models that nonlocal effects are proportional to the surface fluxes may not be valid.

3.3. Local PBL Schemes (TKE Closure) MYJ and Boulac PBL Schemes

[16] Local closure schemes estimate the turbulent fluxes at each grid point from the mean values of atmospheric variables and/or their gradients at that grid point. Because these particular PBL schemes determine eddy diffusion coefficients from prognostic turbulent kinetic energy (TKE), they are also called TKE closure schemes. The governing equations for these TKE closure schemes are:

$$\frac{\partial e}{\partial t} = -\frac{1}{\rho} \frac{\partial}{\partial Z} \rho \overline{w'e'} - \overline{u'w'} \frac{\partial U}{\partial Z} - \overline{v'w'} \frac{\partial V}{\partial Z} + \beta \overline{w'\theta'} - \varepsilon \qquad (4)$$

$$\overline{w'u'} = -K_m \frac{\partial U}{\partial Z} \qquad (5)$$

$$\overline{w'v'} = -K_m \frac{\partial V}{\partial Z} \qquad (6)$$

$$\overline{w'e'} = -K_e \frac{\partial e}{\partial Z} \qquad (7)$$

$$\overline{w'\theta'} = -K_h \frac{\partial \theta}{\partial Z} \qquad (8)$$

where e is the turbulent kinetic energy, β is the buoyancy coefficient and ϵ denotes TKE dissipation by molecular processes. $\left(-\overline{u'w'} \frac{\partial U}{\partial Z} - \overline{v'w'} \frac{\partial V}{\partial Z} \right)$ and $\beta \overline{w'\theta'}$ describe the production of the turbulent kinetic energy due to shear and buoyancy respectively. For the Boulac PBL scheme, in the convective PBL, the countergradient correction term r_{cg} is retained for heat flux component ($\overline{w'\theta'}$) as a constant to accord with *Deardorff* [1972] $\overline{w'\theta'} = -K_h \left(\frac{\partial \theta}{\partial Z} - \gamma_{cg} \right)$. Since this term is treated as a constant and is included in heat mixing in the CBL only, it probably exerts little nonlocal impact [*Bougeault and Lacarrére*, 1989] and we regard Boulac as a local PBL scheme in this study.

[17] The diffusivity in TKE closure schemes is expressed as

$$K_c = S_c l e^{1/2} \qquad (9)$$

where S_c is a numerical coefficient and l is the master length scale. In Boulac PBL scheme, the vertical diffusion coefficient for momentum (K_m), the coefficient for heat (K_h) and the coefficient for TKE (K_e) are identical. In MYJ PBL scheme, they differ from each other. The two TKE closure schemes also differ in how they define S_c and l [*Janjić*, 1990; *Bougeault and Lacarrére*, 1989]. Since turbulence characteristics within and above the PBL are not treated separately, these two TKE closure schemes are based upon local eddy diffusivity for all vertical levels.

[18] In addition, each of the four PBL schemes devises its own technique to diagnose PBL heights. Details are presented in section 4.4.

3.4. Surface Layer Schemes

[19] The surface layer schemes compute friction velocities u_* and exchange coefficients for the computation of surface heat and moisture fluxes by the land surface models and surface stress in the PBL schemes. Over water surfaces, the surface fluxes and surface diagnostic fields are computed in the surface layer scheme itself. It should be noted that there are limitations to the allowable combination between PBL schemes and surface layer schemes. The YSU and ACM2 PBL schemes can be coupled with the MM5-similarity surface layer scheme [*Zhang and Anthes*, 1982]. The MYJ PBL
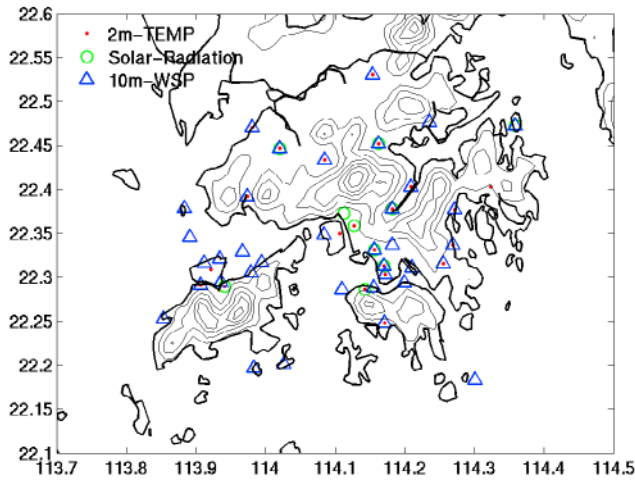
Figure 2. Spatial distribution of observation sites in Hong Kong.

scheme can be coupled only with the Eta-similarity surface layer scheme [*Janjić*, 1996]. The Boulac PBL scheme can be coupled with both MM5- and Eta-similarity surface layer schemes. Therefore the differences introduced by MM5- and Eta-similarity surface layer schemes are also discussed in this study.

4. Results and Discussions

4.1. Period Selection

[20] Hong Kong during summer is dominated by south monsoon winds and during winter is dominated by northeast monsoon winds following climatic patterns common in East Asia. Two simulation periods are selected to represent the summer and winter conditions. According to Hong Kong Observatory, June is representative for summer and November is representative for winter in Hong Kong. The winter simulation period is from 8 A.M., 07th November to 0 A.M., 30th November, 2006, while the summer simulation period is from 8 A.M., 1st June to 0 A.M., 30th June, 2006, local standard time (LST). During the first few days in November, Hong Kong was influenced by the remnants of super typhoon Cimaron. Since the current PBL parameterizations are not designed for reproducing typhoon processes, evaluation of PBL schemes under such a large synoptic forcing is beyond our focus. Therefore, the first part of November is not included in the analyses.

4.2. Surface Meteorological Performances

4.2.1. The 2 m Temperature

[21] Model output of 2 m temperature is evaluated by directly comparing observation data with the value of the nearest grid point at 1 km resolution. As a result, measurements from 23 observation sites in Hong Kong are selected as basis for evaluating model performances in 2 m temperature. In Figure 2, the red dots indicate the observation sites where 2 m temperature is measured.

[22] From the mean time series plots of 2 m temperature, which is averaged spatially over 23 Hong Kong stations in both June and November (Figure 3), it can be seen that although all the PBL schemes show cold biases compared with observations, ACM2 has the best agreement with observation

as well as the smallest cold bias in both June and November. Local PBL schemes MYJ and Boulac always estimate lower 2 m temperatures in Hong Kong geographic region during the nighttime than the nonlocal PBL schemes YSU and ACM2 (not shown here), and local PBL schemes significantly underestimate nocturnal 2 m temperature in comparison with the measurements. MYJ's coldest bias in November and second coldest bias in June is partially attributable to its persistent underestimation of nocturnal 2 m temperature.

[23] Table 1 summarizes the statistical results of model performances in 2 m temperature. Five statistical terms, coefficient of determination, index of agreement (IOA), root mean squared error (RMSE), normalized mean bias (NMB) and normalized mean error (NME) are calculated to evaluate the model performances [*Kwok et al.*, 2010]. By setting the ACM2 simulation as the base case, in June, MYJ's RMSE is higher by 14%, YSU's RMSE is higher by 5% and Boulac's RMSE is higher by 4%. In this summer month, YSU produces the coldest bias because it under-predicts temperature in the daytime to a larger extent compared with other three PBL schemes. In November, in comparison to ACM2's result, YSU's RMSE is higher by 4% while MYJ's RMSE is higher by 26% and Boulac's RMSE is higher by 16%. RMSE with all the other statistical variables in Table 1 indicate noticeable improvements in 2 m temperature simulated by nonlocal PBL schemes (ACM2 and YSU). Overall, all models simulate 2 m temperature better and have a smaller negative bias in November than in June. In comparison with measurements, ACM2 performs best with the smallest underestimation while MYJ gives the worst performance with the largest underestimation in simulating 2 m temperature over the two months.

[24] Regardless of the choice of PBL schemes, the model consistently underestimates nocturnal temperature during most of the days in the two months, although nonlocal schemes (YSU and ACM2) underestimate it to a smaller degree. This fact implies that the underestimation in nocturnal temperature is attributable to the model's weaknesses (for instance, soil moisture adjustment) yet to be resolved.

4.2.1.1. Energy Budget

[25] In the NOAH land surface model, five thermal quantities determine the energy balance equations [*Chen and Dudhia*, 2001]: (1) shortwave radiation including downward shortwave radiation (R_{sd}) and reflected shortwave radiation (R_{su}); (2) long wave radiation including downward radiation emitted by cloud and greenhouse gases (R_{ld}), upward radiation emitted by surface (R_{lu}); (3) sensible heat flux (*HFX*); (4) latent heat flux for evaporation (*LH*); and (5) ground heat flux between surface and soil (*G*).

[26] With reference to *Chen and Dudhia* [2001] and *Mahrt and Ek* [1984], if not considering precipitation or snow (negligible during the study periods), the energy balance equations are:

$$R_n + G - HFX - LH = 0 \qquad (10)$$

$$R_n = R_{sd} - R_{su} + R_{ld} - R_{lu} \qquad (11)$$

$$R_{su} = albedo \times R_{sd} \qquad (12)$$

where R_n is the net radiation, its value being positive with downward direction, and *G* represents ground heat flux, its
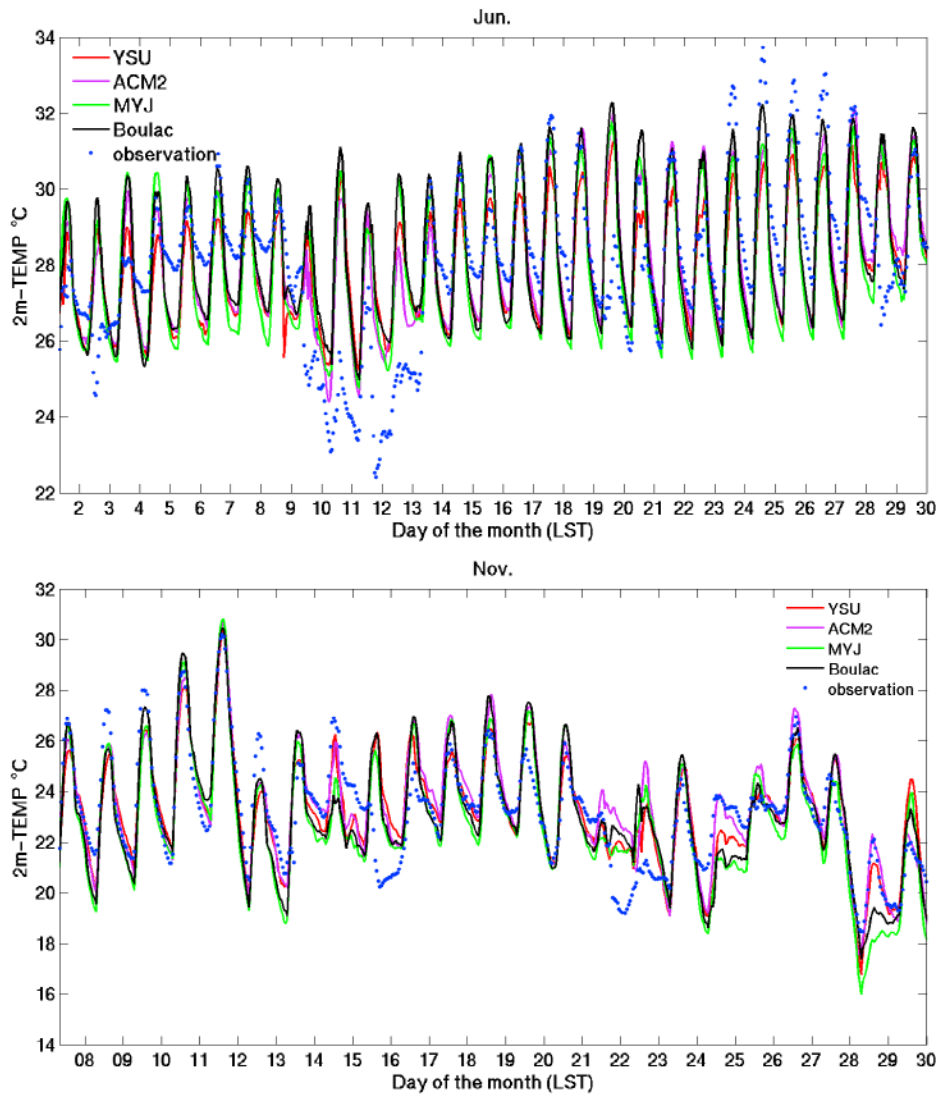
Figure 3. Mean time series of 2 m temperature over 23 sites in Jun and Nov 2006.

value positive when it is transported from soil to surface. *HFX* and *LH* have positive values when they are transported from surface to atmosphere.

4.2.1.2. Comparison Between YSU and ACM2 in 2 m Temperature

[27] YSU and ACM2 scenarios are compared first since they are both run in conjunction with the MM5-similarity surface layer scheme, which means except for variation in the choice of PBL schemes, these two runs have exactly the same configuration. Since the driving forcing is solar radiation, based on the above energy balance equations, the relationship between surface skin temperature and incoming radiation which includes absorbed solar radiation and downward longwave radiation at the surface is investigated.

[28] The November case is used to present a comprehensive analysis regarding the heat exchange at and near the land surface. All the analyses below are based on the averaged results over the 23 stations. In Figure 4, it is obvious that during daytime, the difference in surface skin temperature (TSK) is highly correlated with difference in incoming radiation. The ACM2 scenario generally receives more

Table 1. Model Performance in T2 for 1 km WRF Simulations Over the Period of 8 A.M., 1st Jun to 0 A.M., 30th Jun and the Period of 8 A.M., 07th Nov to 0 A.M., 30th Nov, 2006[a]

	YSU	ACM2	MYJ	Boulac-Eta	Boulac-MM5
2 m Temperature (Celsius) in June					
Determination	0.51	0.51	0.47	0.51	**0.53**
Index of agreement	0.76	**0.80**	0.77	**0.80**	**0.80**
RMSE	1.54	1.47	1.68	1.53	**1.46**
NMB	−0.026	**−0.013**	−0.023	−0.012	−0.018
NME	0.044	**0.040**	0.048	0.042	0.041
2 m Temperature (Celsius) in November					
Determination	0.71	**0.75**	0.70	0.70	0.72
Index of agreement	0.90	**0.91**	0.88	0.89	**0.91**
RMSE	1.33	**1.28**	1.61	1.48	1.32
NMB	−0.008	**0.000**	−0.026	−0.014	−0.005
NME	0.045	**0.043**	0.056	0.050	0.044

[a]Rainy days are excluded; boldface indicates the best one among the different runs.
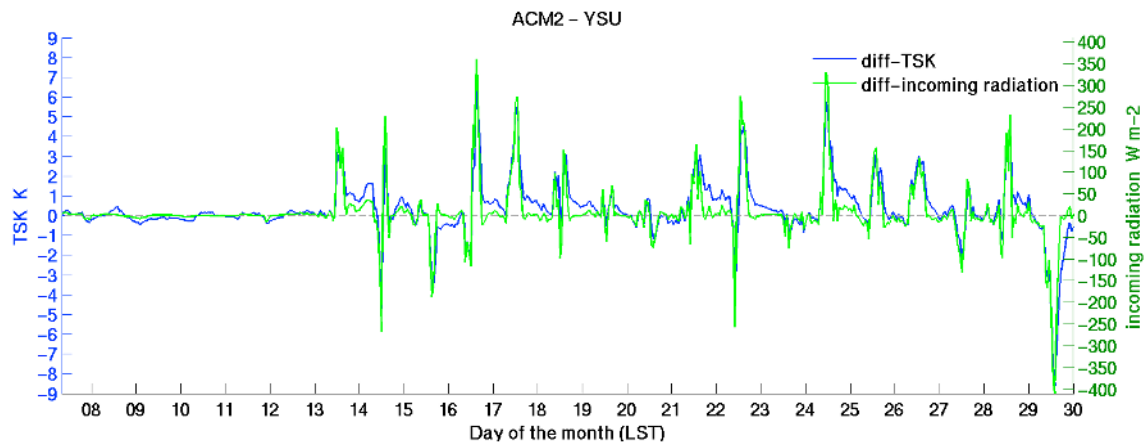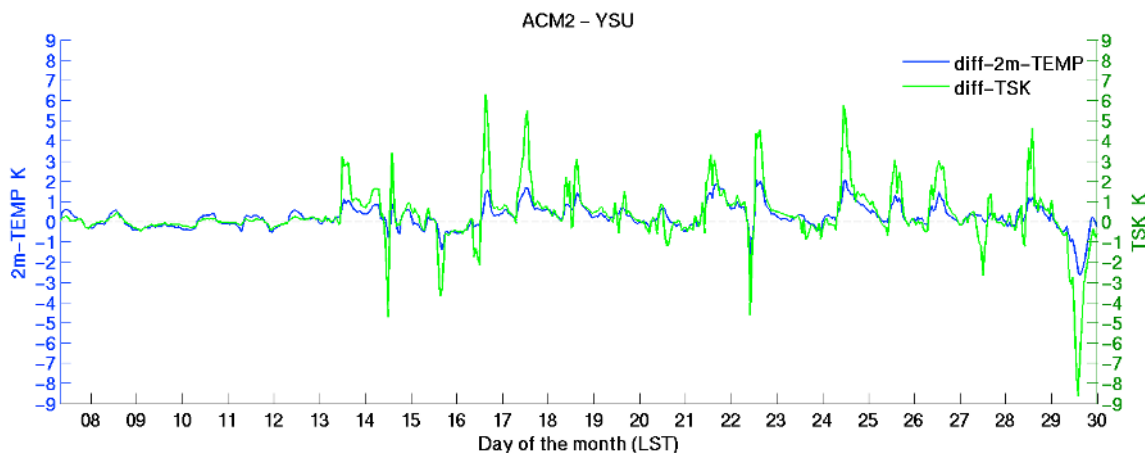
Figure 4. Mean time series of difference (ACM2-YSU) in surface skin temperature (TSK blue line) and difference (ACM2-YSU) in incoming radiation (green line) in November.

incoming radiation, resulting in a higher surface skin temperature than YSU. But in the nighttime, even with little difference in incoming radiation, there is still a relatively large difference in surface skin temperature between YSU and ACM2. This is because in the daytime, when the surface absorbs more radiation in the ACM2 run, a warmer underground soil temperature is produced. After sunset, when the difference in sensible heat flux, latent heat flux and other heat exchange processes between YSU and ACM2 are slight, the process of ground heat flux determines the surface skin temperature. The aforementioned warmer underground soil in the ACM2 scenario (not shown here) would transport upward ground heat flux to the surface and generate a warmer surface skin temperature than that of YSU during the nighttime. Since super typhoon Cimaron started to recede from Hong Kong on 8th Nov, all the model runs with different PBL schemes produce clear sky conditions for the following few days. Consequently differences of incoming radiation and temperatures between YSU and ACM2 in Figures 4 and 5 are small during those days.

[29] From Figure 5, we can detect that difference in 2 m temperature between YSU and ACM2 varies positively with difference in surface skin temperature but with a smaller variance and fewer spikes. Namely, 2 m temperature changes less drastically between PBL schemes. This is because 2 m temperature computed in similarity theory is different from surface skin temperature, which solely depends on column energy budget. In summary, the main cause for a generally higher simulated 2 m temperature and surface skin temperature in the ACM2 scenario is more simulated incoming radiation compared to that in YSU. The next section will explore the reasons for the two nonlocal PBL simulations to reproduce different incoming radiations.

[30] *Cloud impact on incoming radiation at surface.* Incoming radiation is composed of downward shortwave radiation (excluding reflected shortwave radiation by surface) and downward longwave radiation emitted by cloud and greenhouse gases. PBL schemes interact with cumulus schemes, microphysics schemes and land surface models to promote different cloud coverage as a function of time and

Figure 5. Mean time series of difference (ACM2-YSU) in 2 m temperature (blue line) and difference (ACM2-YSU) in surface skin temperature (TSK green line) in November.
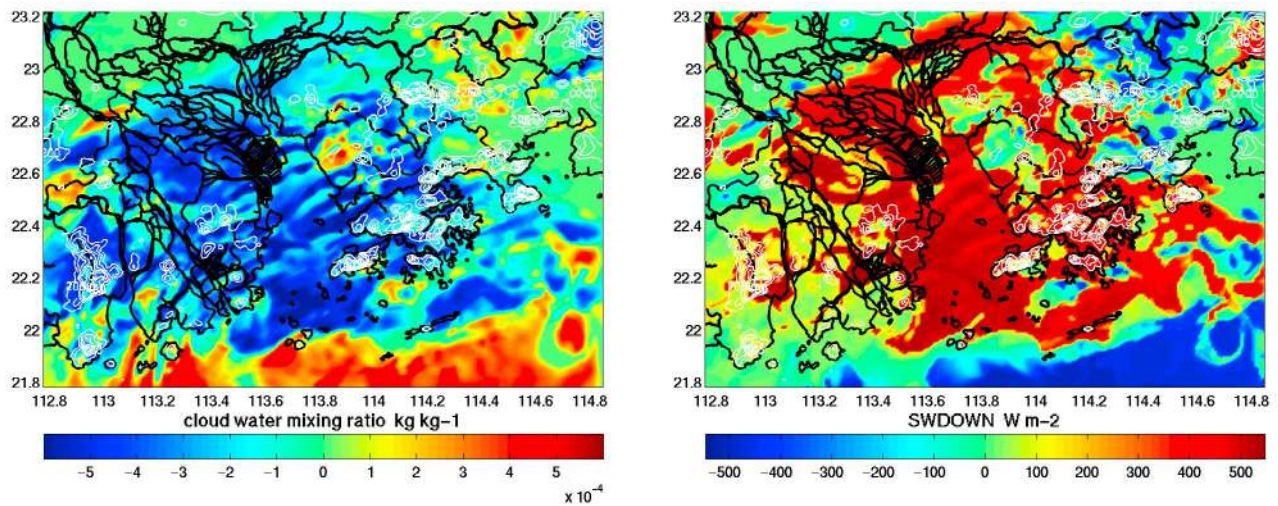
Figure 6. Spatial plot of (left) difference (ACM2-YSU) in cloud water mixing ratio and (right) difference (ACM2-YSU) in downward shortwave radiation (SWDOWN) at 3 P.M., 16th November, 2006.

space. The WRF output variable "cloud water mixing ratio" can represent cloud coverage and intensity. Broad and dense cloud covers can be expected to weaken downward shortwave radiation and strengthen downward longwave radiation. A negative correlation between cloud water mixing ratio and downward shortwave radiation and a positive correlation between cloud water mixing ratio and downward longwave radiation are observed in the model results (not shown here). The impact of cloud cover on radiation is further illustrated in the spatial plot of difference in cloud water mixing ratio and difference in downward shortwave radiation. Occasionally, the difference in incoming radiation can be as large as 500 Wm^{-2} in a large expanse of the Pearl River delta attributable primarily to the selection of PBL schemes (Figure 6).

[31] It is concluded that the determining factor for different simulated 2 m temperatures between YSU and ACM2 is incoming radiation which is mainly influenced by cloud

fraction. In Figure 7 the diurnal mean time series of incoming radiation are averaged spatially over 23 stations and temporally over June and November. During both June and November, there is more incoming radiation in ACM2 scenario in the daytime. Therefore, ACM2 predicts higher 2 m temperatures than YSU (Figure 8). In the nighttime, the differences in 2 m temperature and incoming radiation are both very small.

4.2.1.3. Comparison Between ACM2 and Local PBL Schemes (MYJ and Boulac)

[32] When comparing ACM2 against local PBL schemes, weaker correlations are observed between surface skin temperature difference and incoming radiation difference, and between surface skin temperature difference and 2 m temperature difference caused by PBL schemes. Occasionally the correlations can become negative especially in the first few days of November when the difference in incoming radiation is small (Figure 9 and Figure 10). As mentioned in
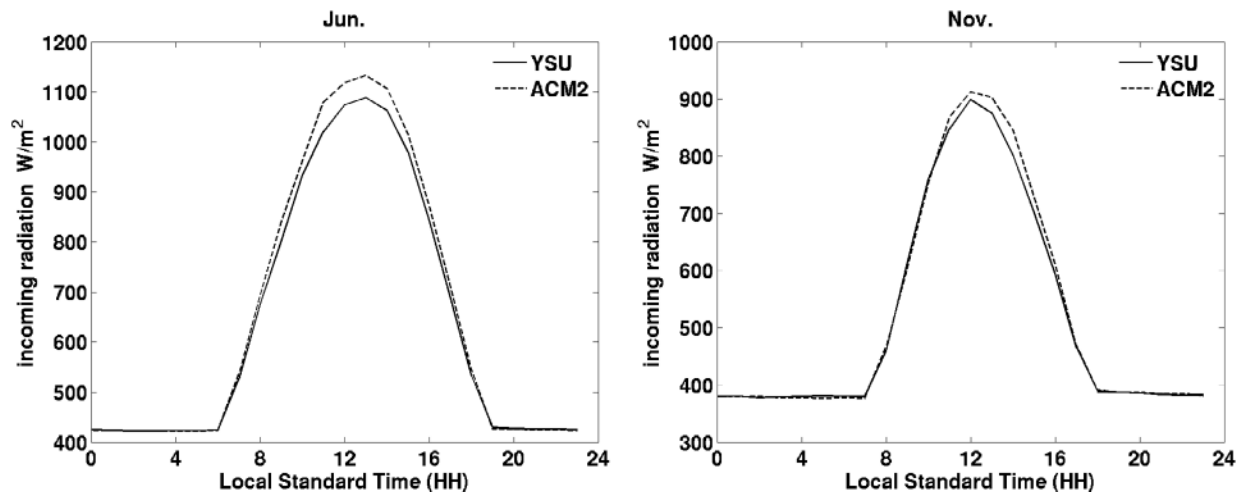
Figure 7. Diurnal mean time series of incoming radiation over 23 stations in Jun and Nov 2006.
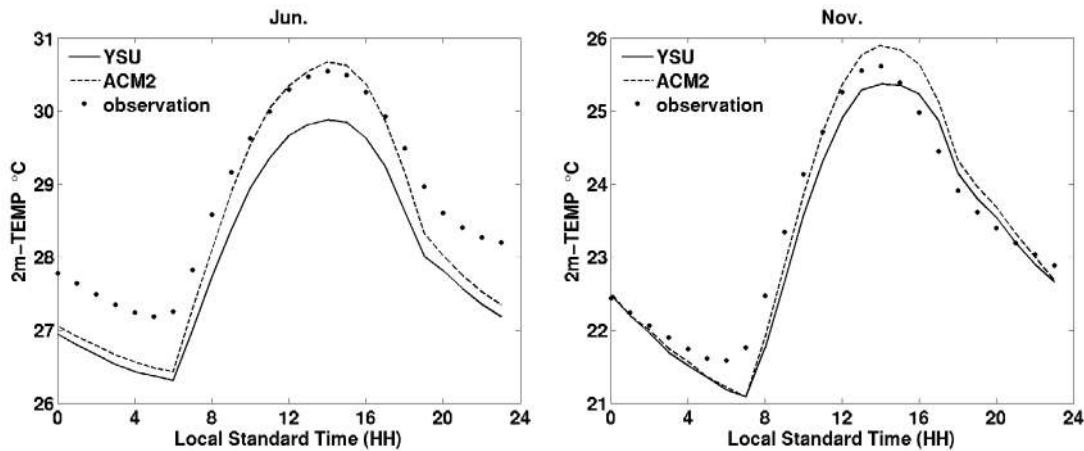
Figure 8. Diurnal mean time series of 2 m temperature over 23 stations in Jun and Nov 2006.

Section 3.4, different surface layer schemes are tied to the PBL schemes. Consequently the variation in exchange coefficients and friction velocity produced by different surface layer schemes can influence modeled sensible heat fluxes, latent heat fluxes and other flux quantities. In the NOAH land surface model, the sensible heat flux is calculated as:

$$HFX = \rho C_p C_h U_1 \left(\theta_{sfc} - \theta_1 \right) \propto C_h U_1 \left(T_{sfc} - T_{2m} \right) \qquad (13)$$

where ρ is the air density, C_p is the specific heat capacity of air at constant pressure, C_h is the surface heat exchange coefficient provided by the surface layer scheme, θ_{sfc} is the surface potential temperature, T_{sfc} and T_{2m} are the surface skin temperature and 2 m temperature, and U_1, θ_1 are atmospheric wind speed and potential temperature at the lowest model layer [*Mahrt and Ek*, 1984; *Chen and Dudhia*, 2001]. 2 m temperature is interpolated between the first model layer and the surface using the similarity theory which is consistent with the surface layer formulation.

[33] Surface wind speeds U_1 are very similar across PBL schemes. This implies that sensible heat flux is primarily dependent on the near surface temperature gradient. An analogous reasoning can be applied to sensible heat flux difference and temperature gradient difference between PBL schemes, provided that the surface heat exchange coefficients C_h are similar. However, a comparison of Figures 11 and 12 shows that the sensible heat flux difference between ACM2 and MYJ is not correlated positively with the near surface temperature gradient difference. A possible explanation is that the MM5-similarity (coupled with ACM2) and Eta-similarity (coupled with MYJ) surface layer schemes produce different surface heat exchange coefficients and proportionality constants to temperature gradient. To quantify the impact of surface layer schemes on 2 m temperature simulation, the Boulac PBL scheme, which can be coupled with the surface layer schemes of interest in this study, is run in conjunction with both the MM5-and Eta-similarity surface layer schemes.

4.2.1.4. Impact of Surface Layer Schemes on 2 m Temperature

[34] The diurnal mean time series in Figures 13–15 are averaged spatially over 23 stations and temporally over June or November. Figure 13 shows that Boulac-Eta scenario
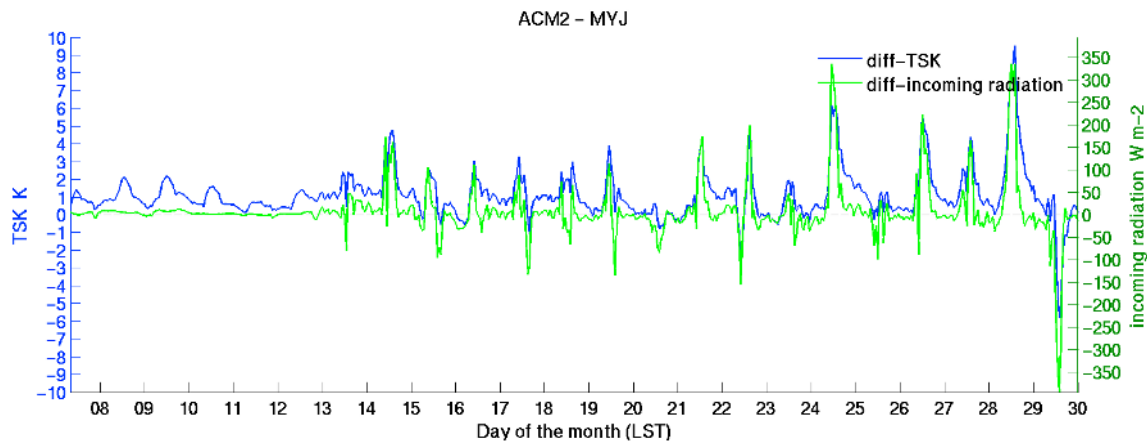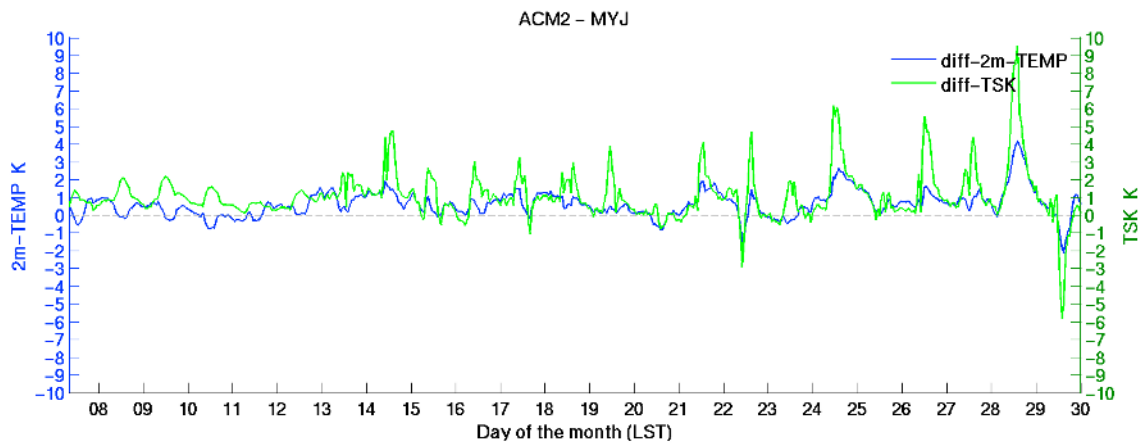

Figure 9. Mean time series of difference (ACM2-MYJ) in surface skin temperature (TSK blue line) and difference (ACM2-MYJ) in incoming radiation (TSK green line) over 23 stations in November.
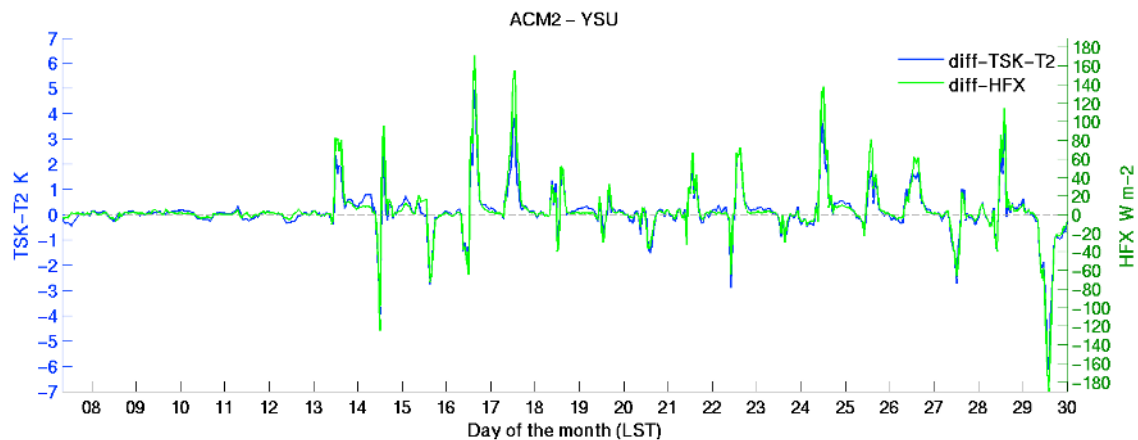
Figure 10. Mean time series of difference (ACM2-MYJ) in 2 m temperature (blue line) and difference (ACM2-MYJ) in surface skin temperature (TSK green line) over 23 stations in November.

produces daytime sensible heat fluxes (*HFX*) similar to that of Boulac-MM5, but smaller daytime near surface temperature gradients. It can be inferred that the Eta-similarity surface layer scheme calculates a significantly larger surface heat exchange coefficient C_h than MM5-similarity surface layer scheme during the daytime. Thus Eta-similarity surface layer scheme would produce a larger sensible heat flux than MM5-similarity surface layer scheme for a given near surface temperature gradient. Nighttime differences in sensible heat flux and near surface temperature gradient between the runs are minimal.

[35] Therefore given differences in C_h during the daytime, different near surface temperature gradients can be maintained in the model. These differences, can then lead to different nighttime simulated temperatures. In June case, incoming radiations (Figure 14) predicted by Boulac-Eta and Boulac-MM5 runs are similar. In the daytime, although a smaller near surface temperature gradient is simulated in Boulac-Eta run, with a much greater C_h, a larger *HFX* is computed in Boula-Eta run in comparison to Boulac-MM5

run. The larger *HFX* (dominant heat flux in the daytime) would give rise to greater energy loss from the surface, hence a lower surface temperature. However, due to the small temperature gradient, a higher air temperature (temperature at 2 m or at the first model layer) is simulated by Eta surface layer scheme. Since the ground heat fluxes are similar between the two runs, a lower surface temperature produces a lower soil temperature in Boulac-Eta run. In the nighttime, when the heat fluxes are similarly weak between Boulac-Eta and Boulac-MM5 runs, the lower soil temperature in Boulac-Eta determines a lower surface temperature, and hence a lower 2 m temperature. Figure 15 depicts the simulated air, surface and soil temperatures in the two runs. Whereas in November case, the lower incoming radiation (Figure 14) predicted by Boulac-Eta obscures the effect of C_h. The lower incoming radiation reduces the surface and air temperatures in Boulac-Eta run. Nevertheless, due to C_h, the simulated daytime 2 m temperature is still higher in Boulac-Eta than that of Boulac-MM5 run, as shown in Figure 15 November case. In statistical terms (Table 1), Boulac-


Figure 11. Mean time series of difference (ACM2-YSU) in surface skin temperature minus 2 m temperature (TSK-T2 blue line) and difference (ACM2-YSU) in sensible heat flux (HFX green line) over 23 stations in November.
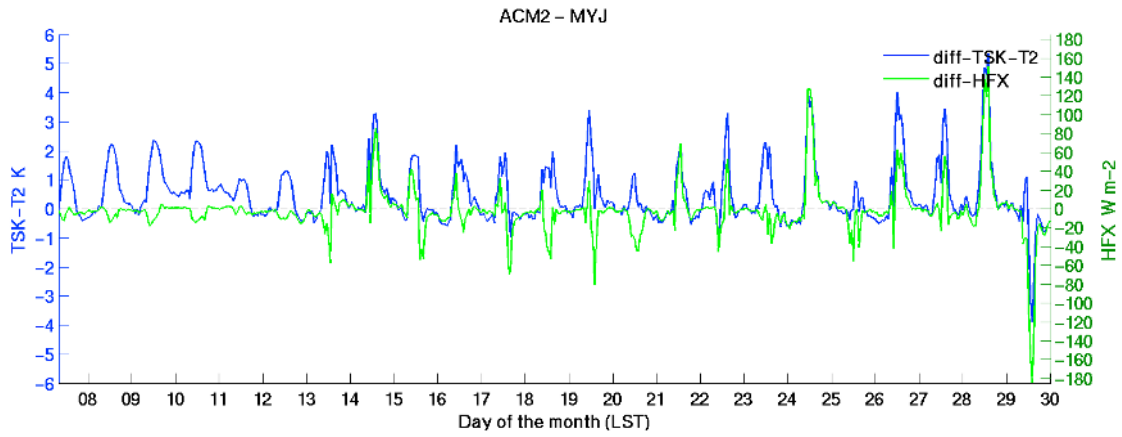
Figure 12. Mean time series of difference (ACM2-MYJ) in surface skin temperature minus 2 m temperature (TSK-T2 blue line) and difference (ACM2-MYJ) in sensible heat flux (HFX green line) over 23 stations in November.
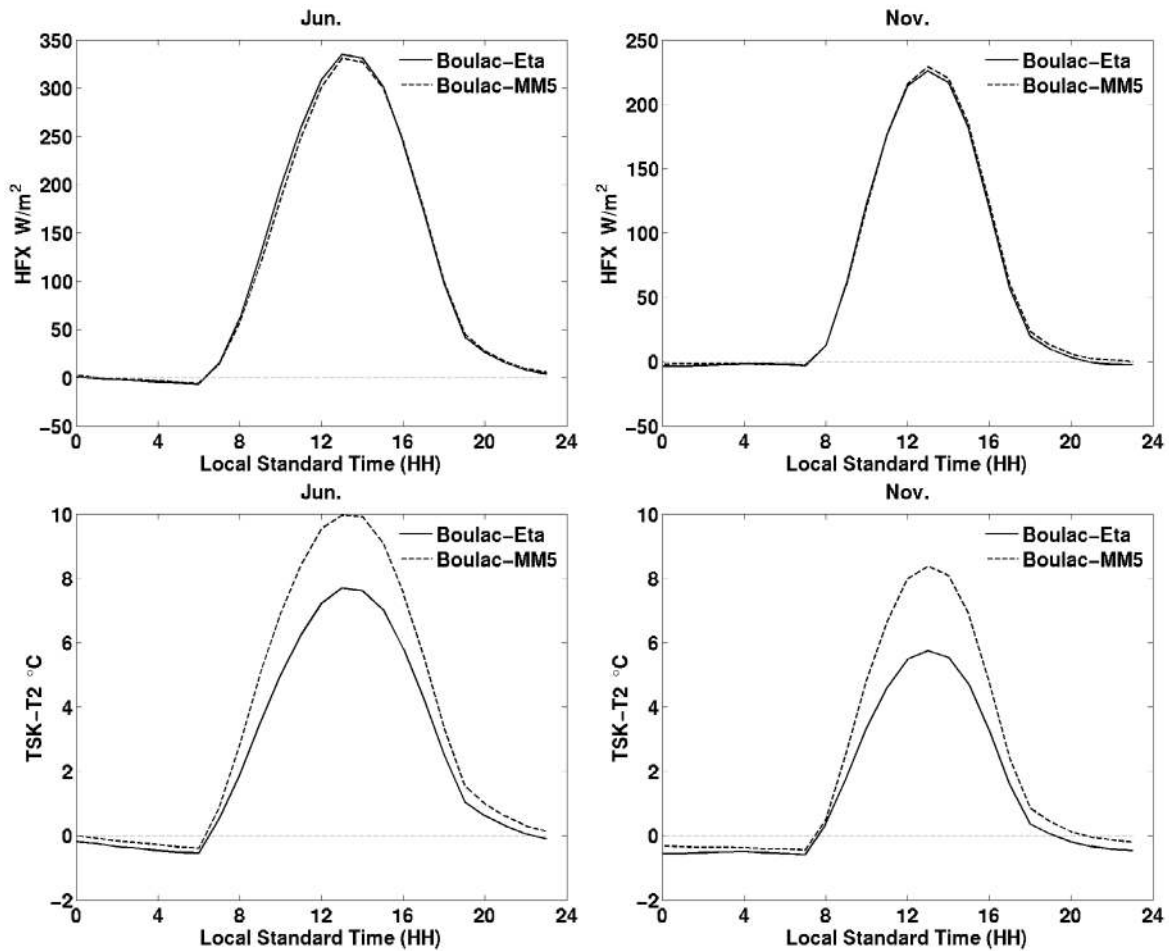
Figure 13. Diurnal mean time series of sensible heat flux (HFX) and surface skin temperature (TSK) minus 2 m temperature (T2) over 23 stations in June and November. (Solid line: Boulac PBL with Eta surface layer scheme, dashed line: Boulac PBL with MM5 surface layer scheme.)
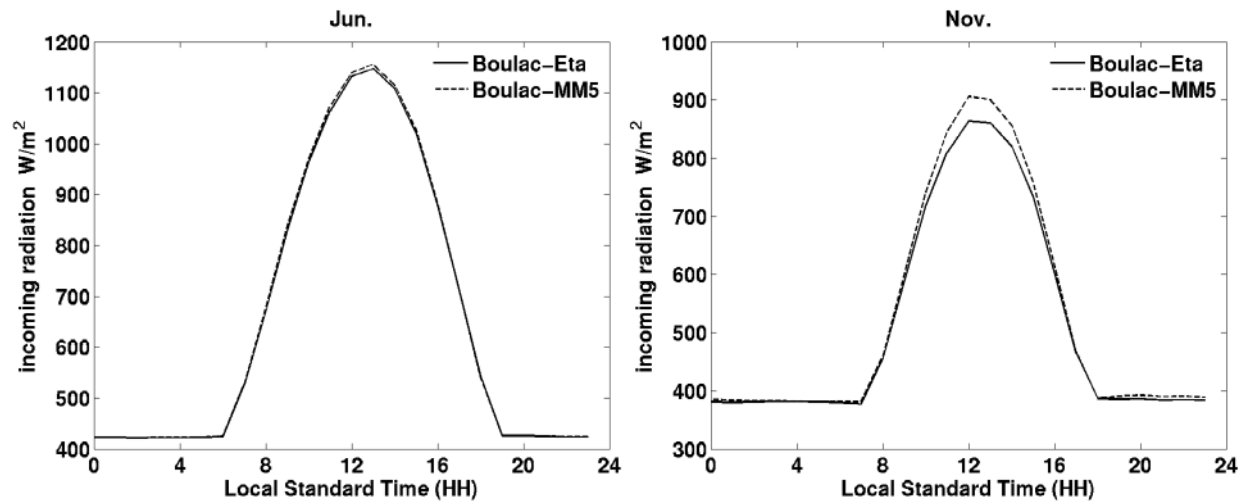
Figure 14. Diurnal mean time series of incoming radiation over 23 stations in (left) June and (right) November. (Solid line: Boulac PBL with Eta surface layer scheme, dashed line: Boulac PBL with MM5 surface layer scheme.)

MM5 scenario has a smaller RMSE in both June and November which indicates a slightly better agreement with the observations than Boulac-Eta scenario.

[36] The impact of surface layer schemes is summarized as follows:

[37] 1. Boulac-Eta generally estimates a lower surface skin temperature and a lower first layer soil temperature than Boulac-MM5 throughout the day in both June and November (Figure 15).

[38] 2. Due to a larger surface heat exchange coefficient C_h in the daytime, Eta-similarity surface layer scheme produces a warmer 2 m temperature in the daytime and a colder 2 m temperature in the nighttime than MM5-similarity (Figure 15). Table 1 summarizes that MM5 surface layer scheme offers a marginal advantage with respect to observed 2 m temperature.

[39] 3. The aforementioned large underestimation of nocturnal 2 m temperature by the local PBL surface layer pairs, MYJ-Eta and Boulac-Eta, as shown in Figure 3, can be partly attributable to physical forcing produced by Eta-similarity surface layer scheme.

4.2.1.5. Discrepancy in 2 m Temperature Caused by PBL Schemes at Selected Times

[40] The episode starts from 8 A.M., November 28th to 0 A.M., November 30th, 2006 (LST), lasting for 40 h. This episode is selected for the following features as illustrated in Figure 16: (1) a large discrepancy exists in simulated 2 m temperature among four PBL schemes, the difference can be as large as 4°C; (2) even between the two nonlocal PBL schemes YSU and ACM2, there is a noticeable difference in 2 m temperature simulation.

[41] As discussed above, solar radiation is the dominant forcing for determining 2 m temperature. Therefore, the simulation of solar radiation directly affects the simulation of 2 m temperature. It is evident in Figure 17 that simulated solar radiation of each scenario deviates sharply from each other. ACM2 consistently presents the best performance to fit with observations and it successfully reproduces the

reduction in solar radiation on 29th November which other PBL schemes fail to do.

4.2.2. The 10 m Wind Speed

[42] Measurements from 40 observation sites in Hong Kong are selected as basis for evaluating the model performances in 10 m wind speed. In Figure 2, the blue triangles denote observation sites where 10 m wind is measured.

[43] The mean time series plots of 10 m wind speed in Figure 18 are averaged over 40 Hong Kong stations in both June and November. In this particular region, mesoscale models have historically been inclined to overestimate wind speed near the surface, especially in highly urbanized areas. During these two months, nonlocal PBL schemes have smaller positive biases with respect to measurements, which mean lower overestimations than local PBL schemes in 10 m wind speed.

[44] Table 2 summarizes the statistical results of 10 m wind speed. Nonlocal PBL schemes exhibit advantage in examined statistical measures, while ACM2 is slightly better than YSU. Compared with ACM2 scenario, in June, MYJ's RMSE is higher by 20% and Boulac's RMSE is higher by 24%. In November, MYJ and Boulac's RMSEs are higher by 21% and 16.9%. RMSE together with other statistical metrics, all indicate noticeably better agreements with measurements by nonlocal PBL schemes (ACM2 and YSU) than local schemes (MYJ and Boulac) in 10 m wind speed simulation. Overall, ACM2 performs best with the smallest overestimation while MYJ gives the worst performance with the largest overestimation compared with 10 m wind speed measurements over the two months.

4.3. Vertical Profiles of Horizontal Velocity, Potential Temperature, Bulk Richardson Number and Water Vapor Mixing Ratio

[45] In air quality modeling context, many research efforts have focused on the evaluation of model performance near the surface, few have concentrated on prognostic skills in reproducing the vertical PBL structure. However, the
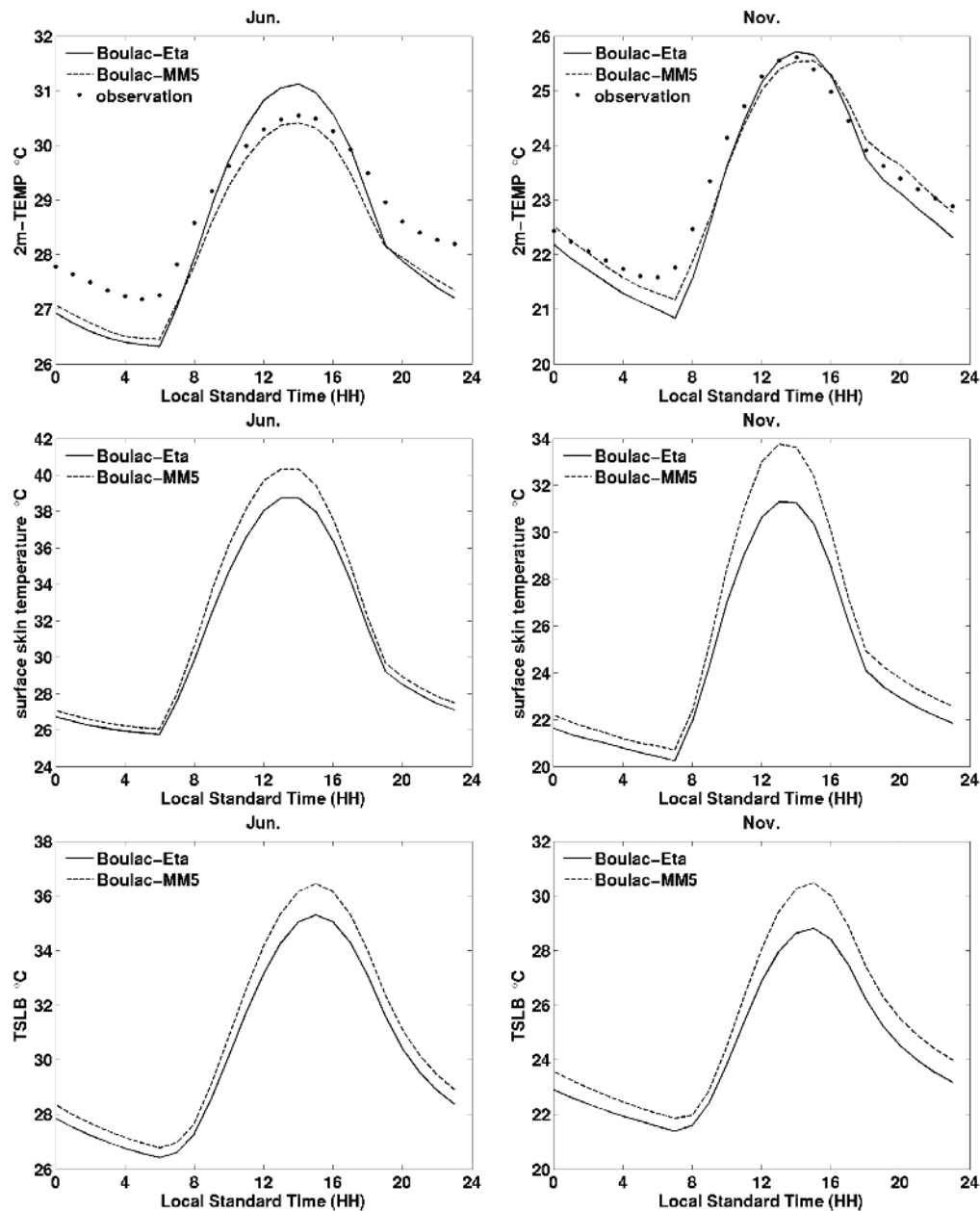
Figure 15. Diurnal mean time series of (top) 2 m temperature, (middle) surface skin temperature, and (bottom) first layer soil temperature (TSLB) over 23 stations in Jun and Nov 2006 (solid line: Boulac PBL with Eta surface layer scheme, dashed line: Boulac PBL with MM5 surface layer scheme).

vertical PBL structure is a key to understanding dynamical meteorology. At a finer scale, the vertical PBL structure is characteristic of turbulent mixing in the atmosphere. Hence, it bares relevance in pollutant transport and dispersion. There is important value, then, in understanding the dependencies between vertical PBL structure and the choice of PBL schemes.

4.3.1. Grid Points Selection in Different Categories and Spatially Averaged Vertical Profiles

[46] To examine vertical profiles of physical properties in the PBL, a form of grid sampling based on land use clustering [*Chan*, 2011] is adopted. We divide the grid points into three categories: urban, rural and ocean. Figure 19 displays the spatial distribution of urban, rural and ocean grid points. In this study, we chose 98 urban grid points and 153 rural grid points and 132 ocean grid points at 1 km resolution within Hong Kong region.

[47] The vertical profiles of horizontal velocity at 2 P.M. on June 8th in Figure 20 are averaged spatially over urban points, rural points and ocean points, respectively. First, although the velocities predicted by different PBL schemes are "convergent" at the surface, the velocities diverge in the upper layers. Over urban points at an altitude of around 600 m AGL, MYJ's horizontal velocity is approximately 1.5 times the magnitude of ACM2's, the difference between these two PBL schemes' predictions is significantly large as
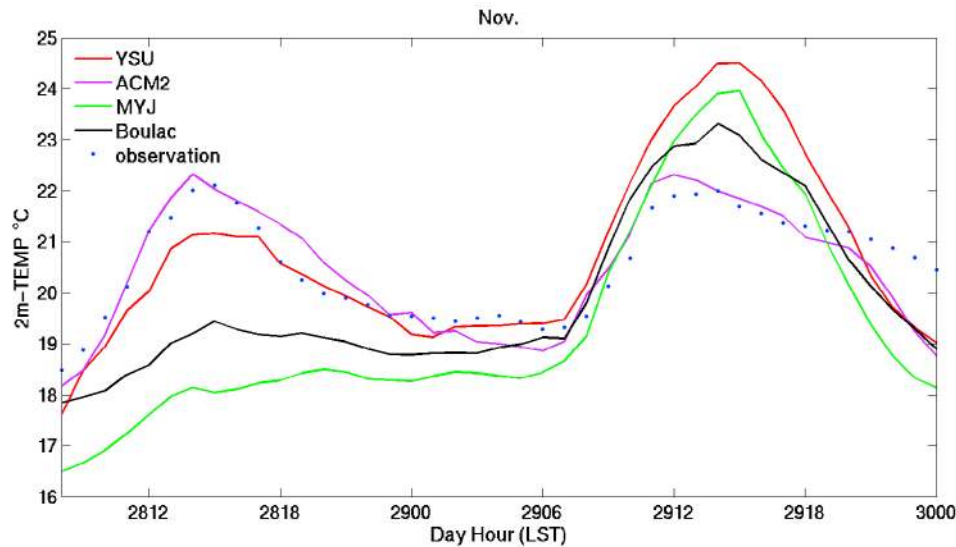
Figure 16. Mean time series of 2 m temperature over 23 sites from 8 A.M., Nov 28th to 0 A.M., Nov 30th, 2006.

5 m/s (55% difference). Each PBL scheme's horizontal velocity evolves with height differently over all land use types. Second, each PBL scheme produces distinct profiles between land (urban and rural) and ocean regions, but produces similar profiles between urban and rural regions. Third, the differences between the profiles over land and over ocean within each PBL scheme are also different from each other between schemes.

[48] The discrepancy in the simulated profile shapes and magnitudes among the various PBL schemes exist not only in horizontal velocity but also in potential temperature and water mixing ratio (not shown here), especially below 1000 m AGL.

4.3.2. Spatially and Temporally Averaged Vertical Profiles

[49] In Figures 21–24, the mean vertical profiles are averaged spatially over each of the three land use categories and hourly over each day's 2 P.M. (representative for the daytime) and over each day's 2 A.M. (representative for the nighttime) in June and November.

[50] In the mean vertical profiles of horizontal velocity (Figure 21), the profile shapes produced by nonlocal schemes (YSU and ACM2) are similar both at 2 P.M. and 2 A.M. The profile shapes produced by the local schemes (MYJ and Boulac) are similar only at 2 P.M. At the surface, the horizontal velocities predicted by all four PBL schemes converge with minor differences. Generally the difference among YSU, ACM2 and MYJ at 2 P.M. (daytime) is larger than that at 2 A.M. (nighttime) over urban and rural region. At 2 P.M., nonlocal schemes produce wind profile with near surface gradients steeper than those of local PBL schemes. ACM2's velocity below 500 m AGL is on average about 0.3 m/s to 1 m/s slower than YSU's. In the upper layers (500 m–1200 m AGL over land, 200 m–600 m AGL over ocean), MYJ's velocity always becomes the largest among the PBL schemes. In other words, MYJ's profile maxima is noticeably stronger than others at 2 P.M. At 2 A.M., the ACM2, YSU and MYJ schemes produce converging wind

profiles over the land. At this time, Boulac, however, produces a wind profile that is dissimilar to those of the other three scenarios. The slow and continuous increase gives rise to persistently smaller velocities in the Boulac scenario than the other three over land within 600 m AGL.

[51] With regard to mean vertical profiles of potential temperature (Theta in Figure 22), the deviation mainly occurs from the surface to about 1000 m AGL. There is a larger difference in potential temperature in November than in June. The mean potential temperatures of nonlocal PBL schemes are noticeably warmer than local PBL schemes within 1000 m AGL in November. MYJ's potential temperature near surface is always the lowest among the four PBL schemes.

[52] To investigate the stability condition within the boundary layer, we calculate the bulk Richardson number layer by layer as follows:

$$R_{ib}(i) = \frac{g(\theta_i - \theta_{i-1})(z_i - z_{i-1})}{\overline{\theta_i}\left[(u_i - u_{i-1})^2 + (v_i - v_{i-1})^2\right]}. \quad (14)$$
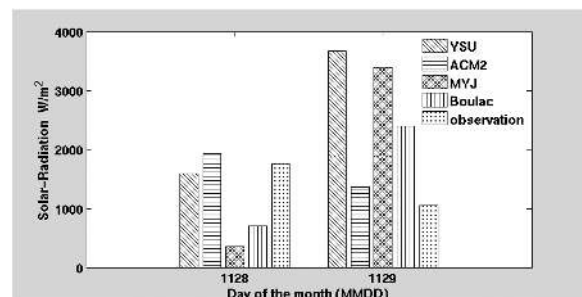
Figure 17. Mean bar chart of daily Solar-Radiation (from 8 A.M. to 6 P.M.) over 10 sites on Nov 28th and Nov 29th, 2006.
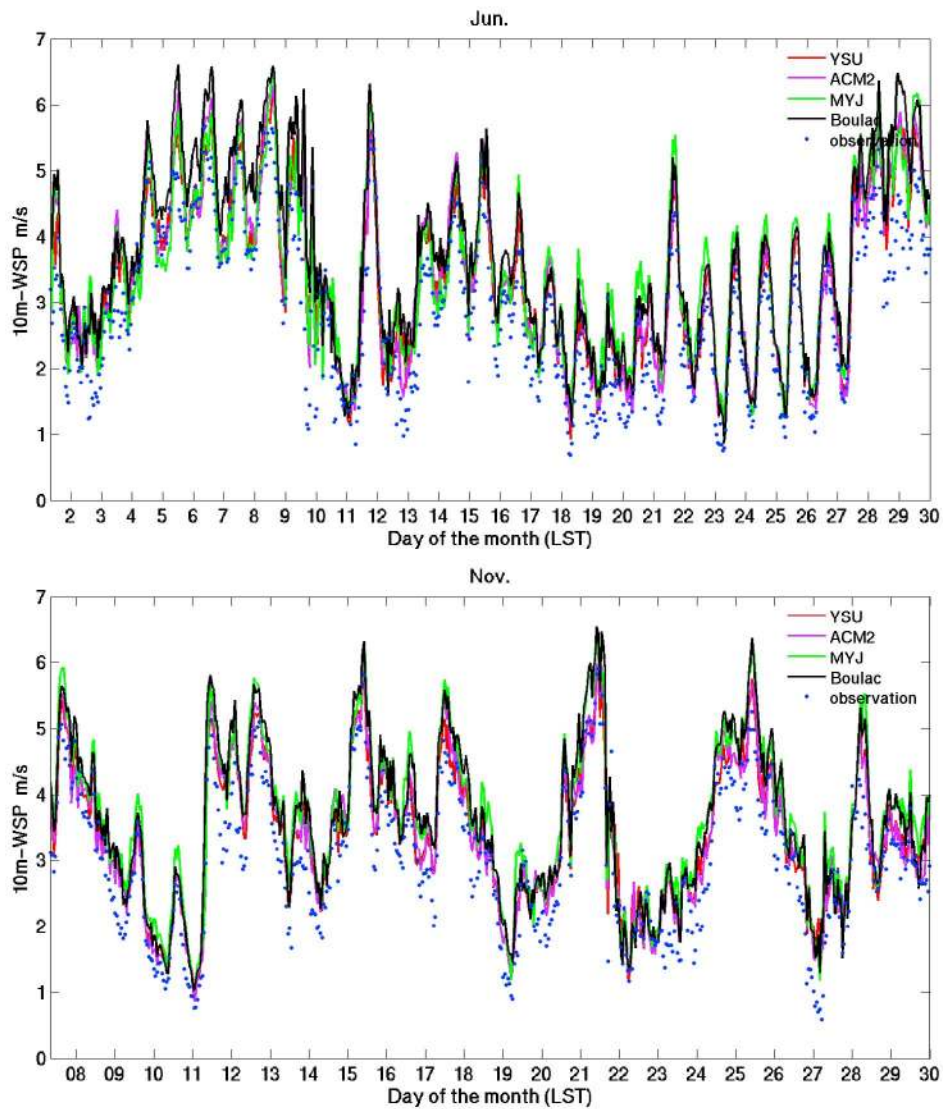
Figure 18. Mean time series of 10 m wind speed (WSP) over 40 sites in Jun and Nov 2006.

$$\overline{\theta_i} = (\theta_i + \theta_{i-1})/2 \qquad (15)$$

where θ_i is the potential temperature at model layer i, $\overline{\theta_i}$ is the mean potential temperature between layer i and layer $i - 1$. g is the acceleration that is due to gravity, z_i is the height at layer i, and u_i and v_i are the zonal and meridian wind components at layer i.

[53] In the lowest model layer, the formula is modified:

$$R_{ib}(1) = \frac{g(\theta_1 - \theta_{2m})z_1}{\left[(u_1)^2 + (v_1)^2\right](\theta_1 - \theta_{2m})/2} \qquad (16)$$

where θ_{2m} is the potential temperature at 2 m, θ_1, z_1, u_1 and v_1 are potential temperature, height, the zonal and meridian wind components at layer 1 respectively.

[54] From equations 14–16, it can be inferred that the sign of per-layer bulk Richardson number depends on the change

Table 2. Model Performance in 10 m Wind Speed for 1 km WRF Simulations Over the Period of 8 A.M., 1st Jun to 0 A.M., 30th Jun and the Period of 8 A.M., 07th Nov to 0 A.M., 30th Nov, 2006[a]

	YSU	ACM2	MYJ	Boulac
10 m Wind Speed (m/s) in June				
Determination	0.55	**0.58**	0.52	0.53
Index of agreement	0.78	**0.79**	0.74	0.74
RMSE	1.34	**1.32**	1.59	1.64
NMB	**0.22**	0.25	0.32	0.38
NME	**0.42**	**0.42**	0.52	0.54
10 m wind speed (m/s) in November				
Determination	0.56	**0.57**	0.53	0.56
Index of agreement	0.79	**0.80**	0.74	0.76
RMSE	**1.27**	1.28	1.54	1.49
NMB	**0.20**	0.21	0.35	0.34
NME	**0.39**	**0.39**	0.51	0.49

[a]Rainy days are excluded; boldface indicates the best one among the different runs.
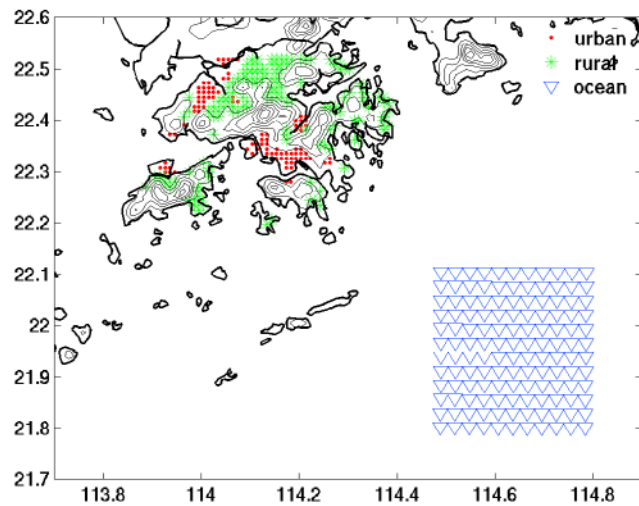
Figure 19. The distribution of urban, rural and ocean points.

of potential temperature between model layer and adjacent lower model layer, but the magnitude of per-layer bulk Richardson number is also a function of change in velocity. From Figure 23, it is found that at 2 P.M. (daytime), YSU and ACM2's profiles show stronger vertical mixing than those of local PBL schemes in the upper layers. ACM2's per-layer bulk Richardson number is always the smallest, which means that it predicts the most turbulent conditions above certain critical heights over land (600 m AGL over urban, 400 m AGL over rural). Whereas, MYJ's per-layer

bulk Richardson number is always larger than that of non-local PBL schemes above that height. Over urban areas, YSU estimates a Richardson number at the second model layer that is much larger than those of the other three PBL schemes. It is possible that the countergradient term γ_c in the YSU diffusion algorithm might have over-diminished the local mixing in the low model layers. Over the ocean, at 2 P. M. in June, the nonlocal PBL schemes are more turbulent than local PBL schemes in the upper layers. But at 2 P.M. in November, the ocean differences among PBL schemes are small. At 2 A.M. (nighttime), small variances exist among the per-layer bulk Richardson number profiles over land, whereas over ocean nonlocal PBL schemes are more turbulent than local PBL schemes in the upper layers.

[55] Figure 24 shows the mean vertical profile of water vapor mixing ratio, Qv. The near surface Qvs are very similar among the four PBL schemes. The profiles variations often appear between 400 m and 1200 m AGL. Within this range of height, the nonlocal PBL schemes always predict higher Qvs than the local PBL schemes. Moreover, the difference in Qv profiles over ocean is often greater than that over land.

[56] To investigate the strengths of capping inversion layers produced by different PBL schemes in the CBL, Figure 25, vertical profiles of theta are plotted as a function of height normalized by the PBL depth. The normalized profiles are then averaged hourly at 2 P.M. over urban, rural and ocean respectively. Therefore the capping inversion layer within PBL corresponds approximately to 0.8–1 in Figure 25. It is noticed that in both June and November, the capping inversion layers produced by nonlocal PBL schemes are stronger than that of local PBL schemes. Over urban and rural, the potential temperatures produced by
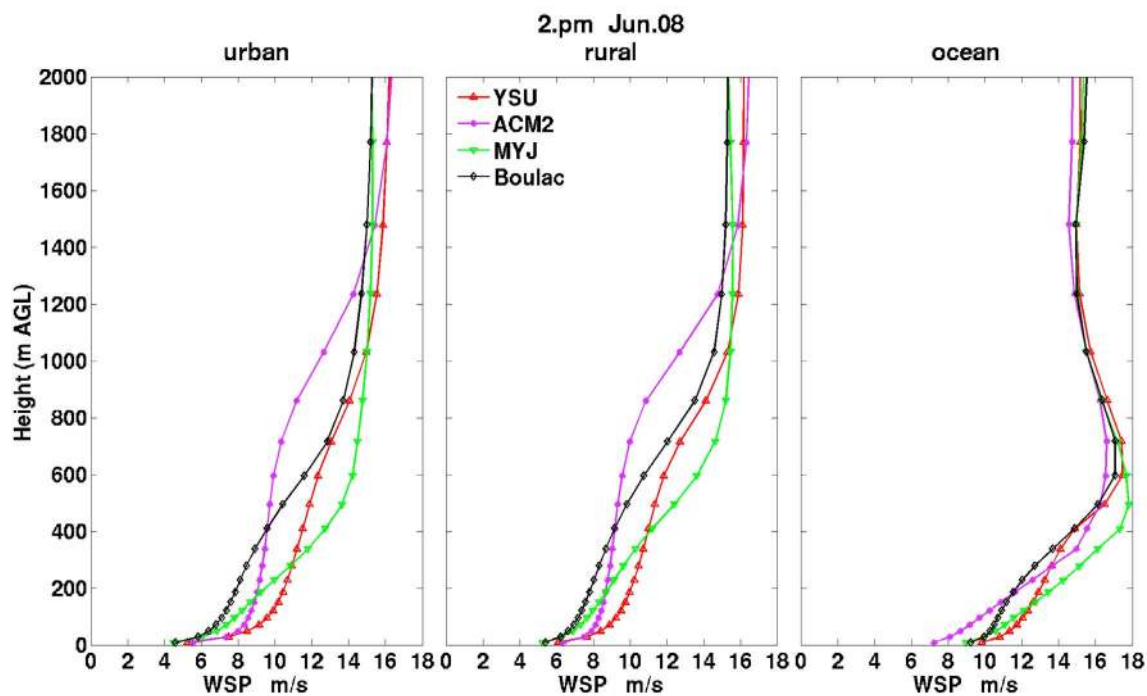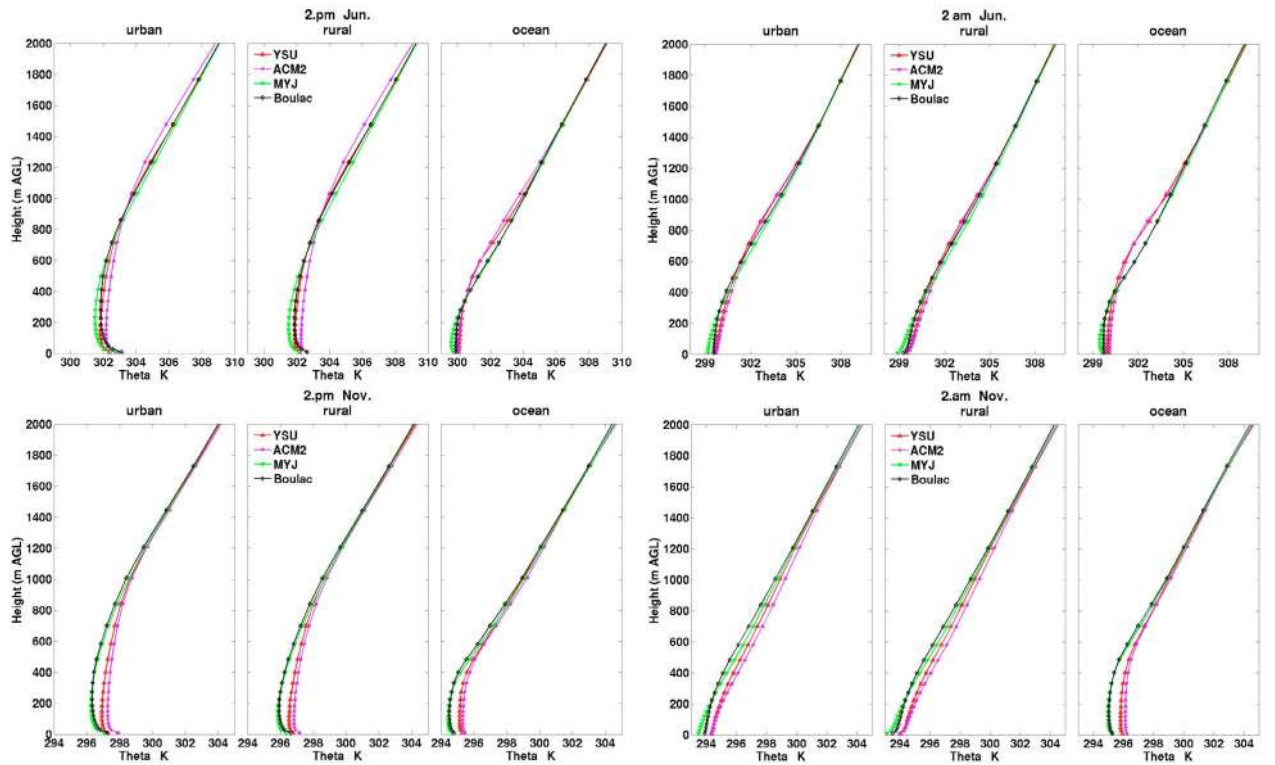

Figure 20. Spatially averaged vertical profiles of horizontal velocity in urban, rural and ocean regions at 2 P.M., June 8th, 2006.
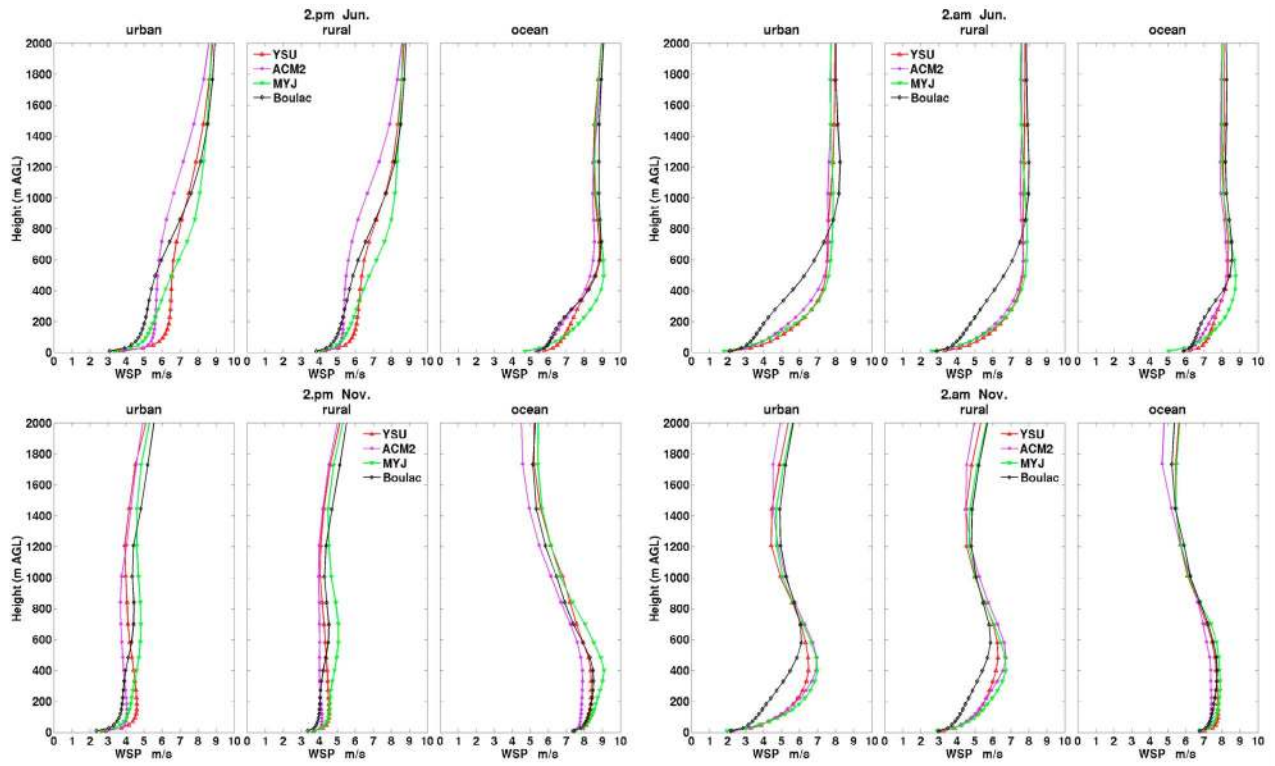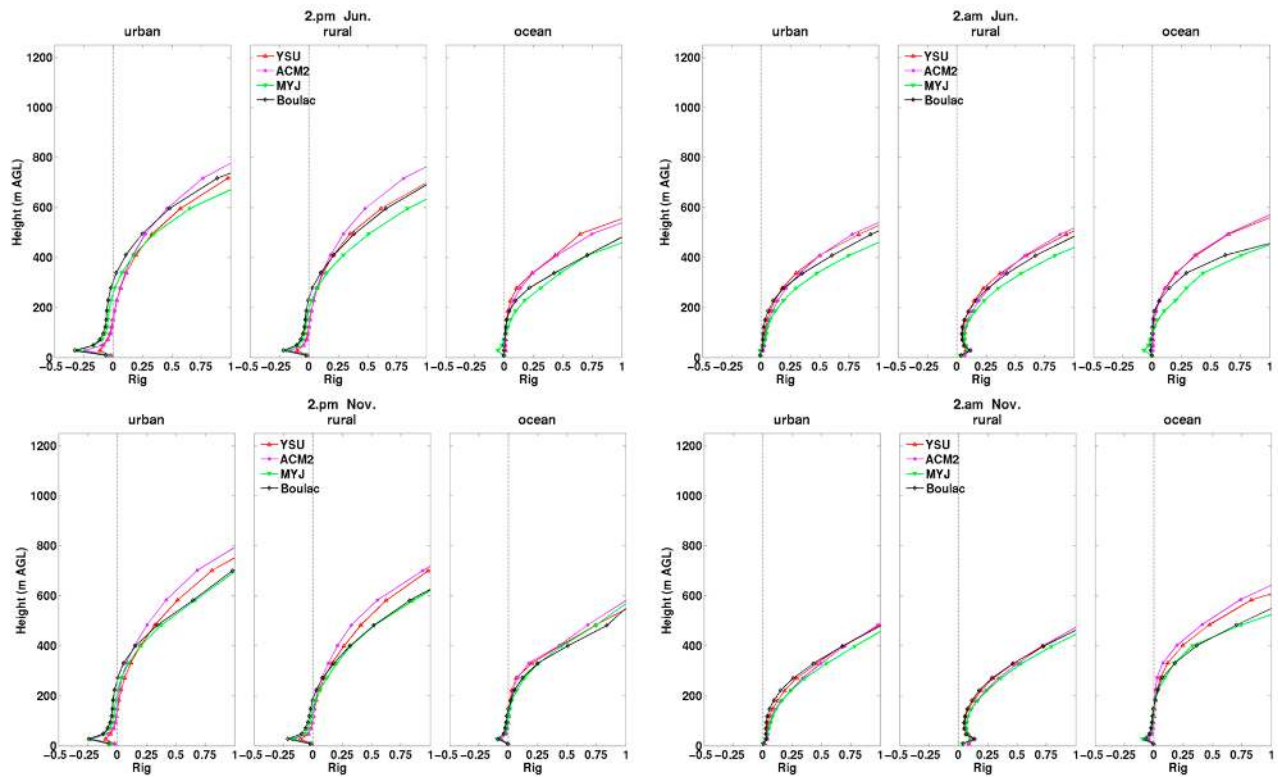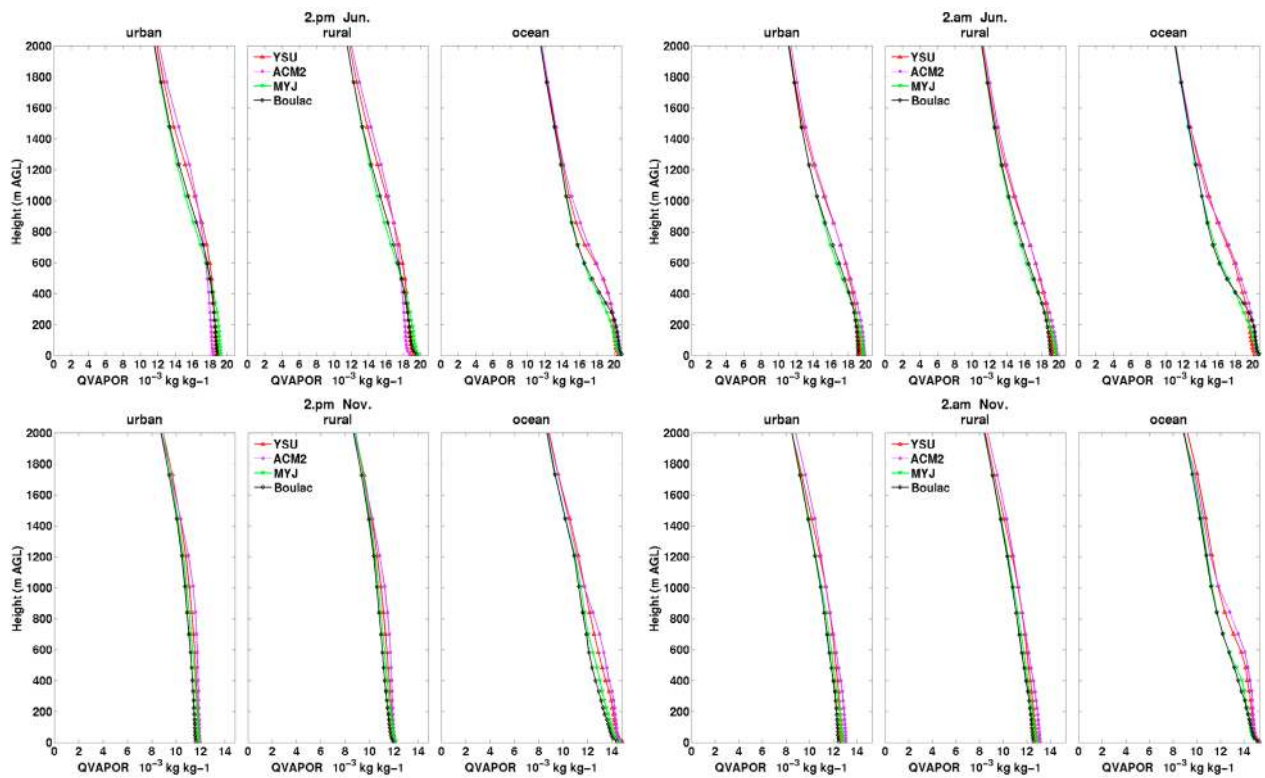
Figure 21. Spatially and hourly averaged vertical profiles of horizontal velocity in urban, rural and ocean regions at 2 P.M. and 2 A.M. over (top) Jun. and (bottom) Nov.

Figure 22. Spatially and hourly averaged vertical profiles of potential temperature in urban, rural and ocean regions at 2 P.M. and 2 A.M. over (top) Jun. and (bottom) Nov.
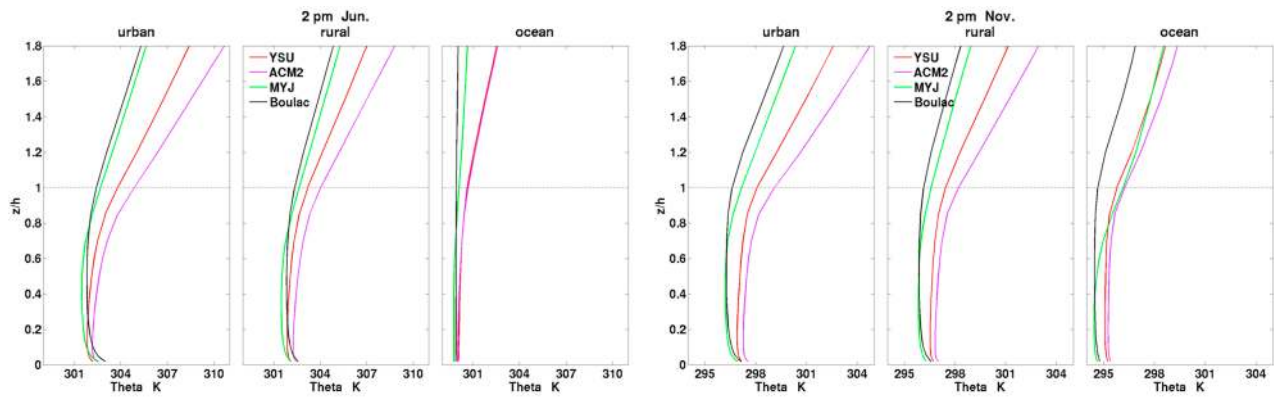
Figure 23.   Spatially and hourly averaged vertical profiles of per-layer bulk Richardson number in urban, rural and ocean regions at 2 P.M. and 2 A.M. over (top) Jun. and (bottom) Nov.

Figure 24.   Spatially and hourly averaged vertical profiles of water vapor mixing ratio in urban, rural and ocean regions at 2 P.M. and 2 A.M. over (top) Jun. and (bottom) Nov.

Figure 25. Spatially and hourly averaged vertical profiles of potential temperature as a function of normalized height in urban, rural and ocean regions at 2 P.M. over (left) Jun. and (right) Nov.

nonlocal PBL schemes are notably higher than that of local PBL schemes above vertical coordinate 0.3. The profiles of nonlocal PBL schemes are similar in form within PBL. Over ocean, the profiles of nonlocal PBL schemes are similar in shapes and also magnitudes. It should be noted that the diagnosed PBL heights in different PBL schemes exhibit considerable differences, which are discussed in section 4.4.

[57] Figure 26 shows the comparisons between model predictions and the available sounding data. The profiles are averaged monthly at station King's Park. All the PBL schemes are capable of capturing temperature and wind speed profiles in the PBL. However, this single sounding station which measures data at two specific times (8 A.M. and 8 P.M. LST) is statistically insufficient to determine
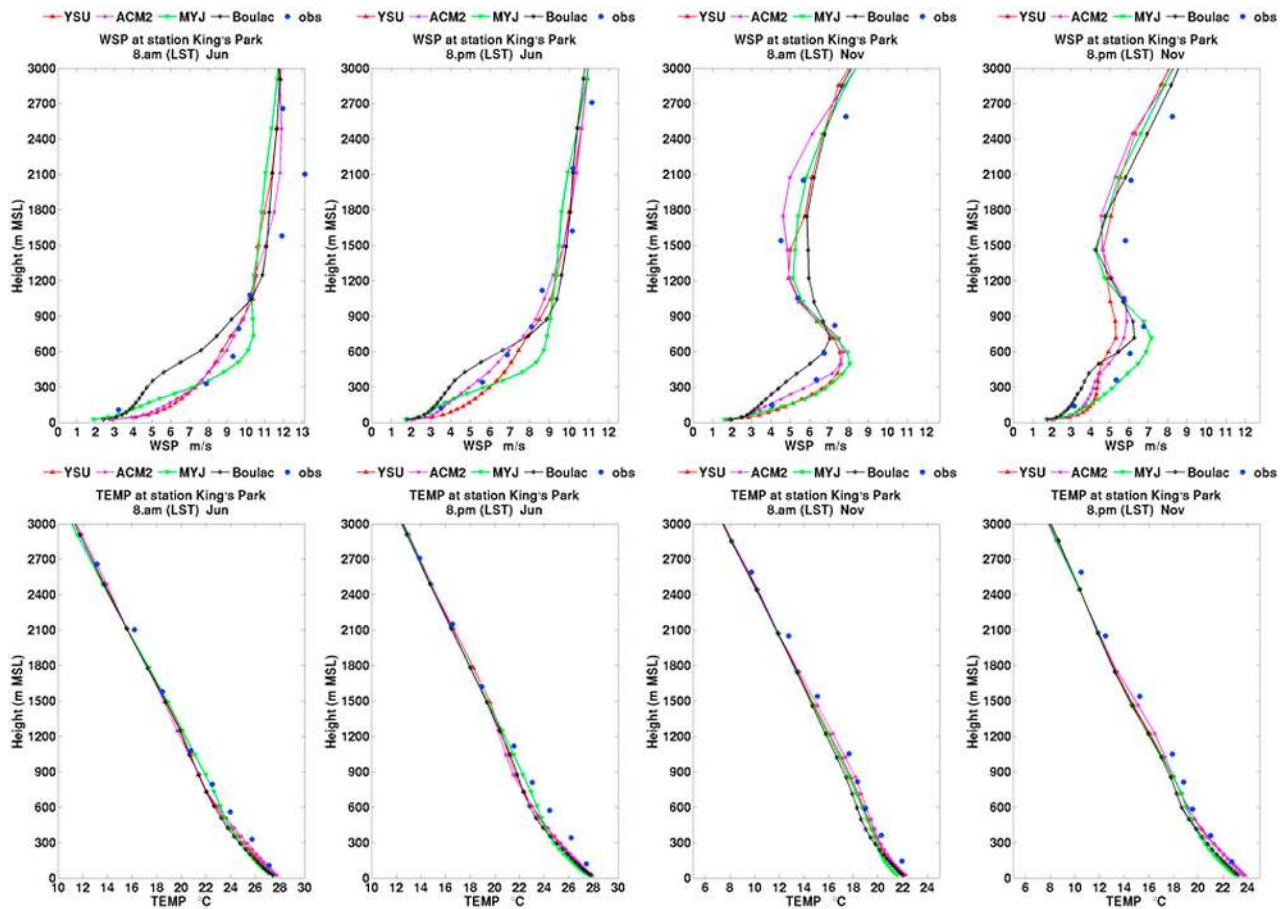
Figure 26. Mean vertical profiles of (top) horizontal velocity and (bottom) temperature at King's Park at 8 A.M. and 8 P.M. over Jun. and Nov.

which PBL scheme performs more realistically. Also, during these observation periods the variance among PBL schemes is notably not as prominent as it would be during daylight hours of peak heating. Thus, a robust verification of PBL profile predictions is predicated upon further availability of spatiotemporal sounding data.

4.3.3. Variances in Vertical Properties Among PBL Schemes

[58] Four statistical perspectives of PBL profile differences among schemes had been analyzed: (1) to quantify hourly profile differences by examining the maximum variance and the average variance for elevations below 1000 m AGL; (2) to delineate variances among PBL schemes in terms of wind speed, theta, and Qv for the vertical spans "near surface" and "upper layers"; (3) to determine the stability conditions which exacerbate PBL profile differences among schemes. For instance, whether the variance during daytime (2 P.M.), when the atmosphere is usually more convective over land, is larger than that in the night (2 A.M.), when the atmosphere is relatively stable over land; and (4) to identify the height of maximum profile variance.

[59] We use the statistical term standard deviation (SD) to quantify the discrepancy in simulated variables. The SD is calculated among the four PBL schemes layer by layer at each day's 2 P.M. and 2 A.M. over different land use types respectively as below:

[61] For all the standard deviations of horizontal velocity, potential temperature and water vapor mixing ratio, we summarize as follows:

[62] 1. The maximum SD values in velocity, theta and Qv are larger than 1.2 m/s, 0.7 K and $0.8 * 10^{-3}$ kg/kg respectively over most days of the entire simulation period. This indicates considerable deviations among vertical profiles predicted by the PBL schemes.

[63] 2. The maximum SD and the mean SD at 2 A.M. are NOT always smaller than those at 2 P.M. The PBL schemes can behave distinctively under unstable and stable conditions.

[64] 3. The magnitudes of the maximum SD and of the mean SD are always similar between urban and rural points, but are different between land (urban and rural) and ocean points.

[65] 4. The maximum SD varies and appears at different heights in each day (not shown here). It is important to be aware that averaging over corresponding hours on each day of the month, shown in Figures 21–24, can obscure profile characteristics that are particular to any given day.

[66] 5. Horizontal velocity and Qv over land are often less variable near the surface than in the upper layers among the PBL schemes.

$$SD(i,k,t) = \sqrt{\left[(YSU(i,k,t) - aver(i,k,t))^2 + (ACM2(i,k,t) - aver(i,k,t))^2 + (MYJ(i,k,t) - aver(i,k,t))^2 + (Boulac(i,k,t) - aver(i,k,t))^2\right]/4}$$

$$aver(i,k,t) = [(YSU(i,k,t) + ACM2(i,k,t) + MYJ(i,k,t) + Boulac(i,k,t))]/4$$

$$SD(lu,k,t) = \sum_{i=1}^{N} SD(i,k,t)/N \tag{17}$$

lu denotes a land use category (urban, rural or ocean), i denotes a grid point belonging to that land use category and N denotes the total number of grid points within that land use category; $YSU(i,k,t)$, $ACM2(i,k,t)$, $MYJ(i,k,t)$ or $Boulac(i,k,t)$ represents the prediction by the corresponding PBL scheme at grid point i, layer k and time t of either 2 P.M. or 2 A.M., and $aver(i,k,t)$ signifies the average prediction of the four PBL schemes at grid point i, layer k and time t.

[60] Equations (18) and (19) are used to quantify the overall extent of deviation in the PBL. Here the maximum standard deviation $SD_{max}(lu,t)$ indicates the largest SD among the vertical layers (17 layers) within 1000 m AGL and the mean standard deviation $\overline{SD(lu,t)}$ denotes the average SD among the vertical layers within 1000 m AGL.

$$SD_{max}(lu,t) = \max[SD(lu,k,t)] \quad k = 1, 2, \ldots, N_k \text{ where } N_k = 17 \tag{18}$$

$$\overline{SD(lu,t)} = \sum_{k=1}^{N_k} SD(lu,k,t)/N_k \quad k = 1, 2, \ldots, N_k \text{ where } N_k = 17 \tag{19}$$

[67] 6. The large discrepancy in these variables exists not only within the PBL but also above the PBL, due to the cumulative PBL effects on the free atmosphere circulation in the model.

4.3.4. Impact of Surface Layer Schemes on Vertical Profiles

[68] The Boulac-Eta (Boulac PBL with Eta surface layer scheme) and Boulac-MM5 (Boulac PBL with MM5 surface layer scheme) runs show that both vertical profiles of theta and Qv are less dependent on surface layer schemes than PBL schemes. Although there are occasional discrepancies between Boulac-Eta and Boulac-MM5 in Qv over ocean points (the difference at one layer can be $5 * 10^{-3}$ kg/kg, not shown here), the insensitivity of these two variables to the surface layer schemes agrees with *Shin and Hong* [2011]. Shin and Hong also indicated that surface layer schemes exert little impact on vertical profiles of horizontal velocity in their one day simulation, which is true during some days in our simulation period. However, we found that horizontal velocity could be fairly sensitive to surface layer schemes, especially at 2 P.M. (daytime). Half of our simulation days exhibit mean standard deviations (averaged among 17 layers within 1000 m AGL) that are larger than 0.5 m/s in horizontal velocity (not shown here). It can be inferred from Figure 27 that the impact of surface layer schemes is not restricted to the near surface variability; it can propagate to
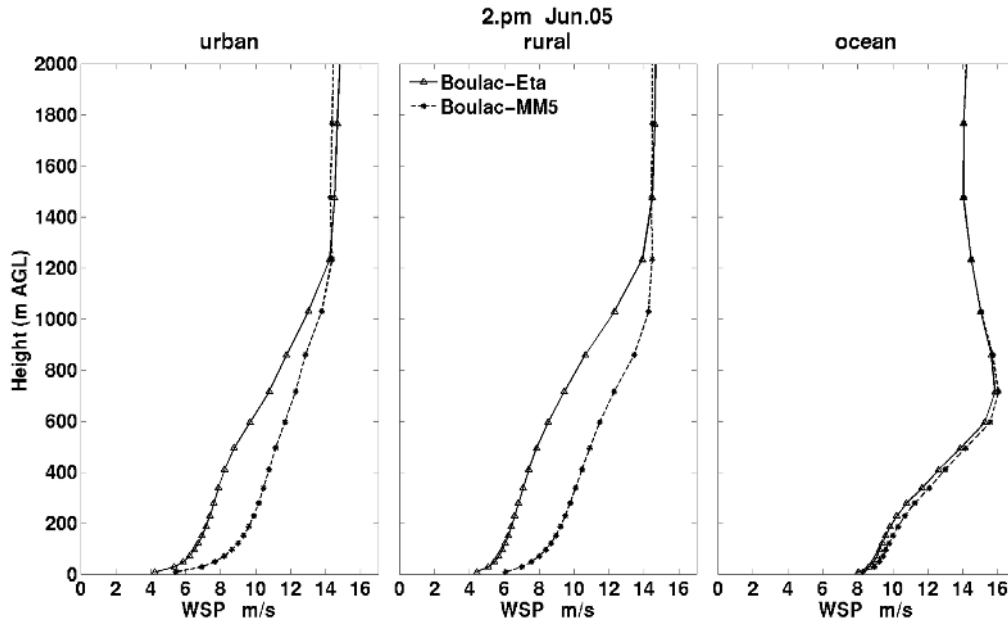
Figure 27. Spatially averaged vertical profiles of horizontal velocity in urban, rural and ocean regions at 2 P.M., June 5th.

the upper layers and alter the shape of the vertical profiles of horizontal velocity.

4.4. PBL Heights

[69] The PBL height is a key variable for air quality modeling. Its accurate simulation is often difficult in numerical models [*Dabberdt et al.*, 2004]. To provide a consistent analysis and correlate the PBL height with temperature over Hong Kong region, predicted PBL height is averaged over 23 observation sites in Hong Kong where 2 m temperature is measured. Figure 28 shows that in both June and in November, ACM2 always produces the largest PBL heights, and YSU the second highest. The local PBL schemes (MYJ and Boulac) predict shallower PBL heights which are almost half the heights predicted by ACM2 run throughout the month. PBL height diagnostic formulation is PBL scheme specific. YSU and ACM2 determine the top of PBL where bulk Richardson number first exceeds a critical value. Specifically YSU calculates the bulk Richardson number starting from the surface. In convective boundary layer, its critical bulk Richardson value is set as zero, while in stable boundary layer, the critical value has been modified from zero to 0.25 over land. This gives rise to enhanced mixing in the stable boundary layer [*Hong et al.*, 2006; *Hong*, 2010]. In the ACM2 diagnostic equation for unstable conditions, *Pleim* [2007a] suggested that the PBL is composed of an entrainment layer situated immediately above a free convective layer. The depth of the free convective layer is defined at the height of neutral buoyancy with respect to the rising plumes below. The depth of the entrainment layer is defined as the differential height between the top of the free convective layer and the point where the entrainment-layer-specific bulk Richardson number reaches a critical value. The PBL height, then, is the sum of the free convective layer and the entrainment layer. For stable conditions,

ACM2 uses a similar method as that in YSU for diagnosis of PBL height:

$$h = Ri_{crit} \frac{\overline{\theta_v}\left([u(h) - u(z_1)]^2 + [v(h) - v(z_1)]^2\right)}{g[\theta_v(h) - \theta_v(z_1)]} \quad (20)$$

where h is the PBL height, θ_v is the virtual potential temperature, z_1 is the height of the lowest model level, $\overline{\theta_v}$ is the average virtual potential temperature between the layer 1 and h, $u(h)$ and $v(h)$ are the wind at height h, and Ri_{crit} is the critical bulk Richardson number defined as 0.25.

[70] For unstable conditions, ACM2 applies the bulk Richardson number method over the entrainment layer only. First the top of the convectively unstable layer (z_{mix}) is found as the height at which $\theta_v(z_{mix}) = \theta_s$:

$$\theta_s = \theta_v(z_1) + b\frac{\overline{(w'\theta'_v)_o}}{w_m} \quad (21)$$

where b = 8.5 and $\overline{(w'\theta'_v)_o}$ represents surface kinematic heat flux. The bulk Richardson number is then defined for the entrainment layer above z_{mix} such that

$$Ri_b = \frac{g[\theta_v(h) - \theta_s](h - z_{mix})}{\overline{\theta_v}\left([u(h) - u(z_{mix})]^2 + [v(h) - v(z_{mix})]^2\right)} \quad (22)$$

[71] The PBL height h is diagnosed when Ri_b equals to Ri_{crit} which is 0.25 in WRF ACM2 PBL [*Pleim*, 2007a, 2007b].

[72] Local PBL schemes (MYJ and Boulac) define the PBL height where turbulent kinetic energy decreases to a prescribed value 0.1 m^2/s^2 for MYJ and Boulac [*Janjić*, 2002; *Bougeault and Lacarrére*, 1989]. To illustrate
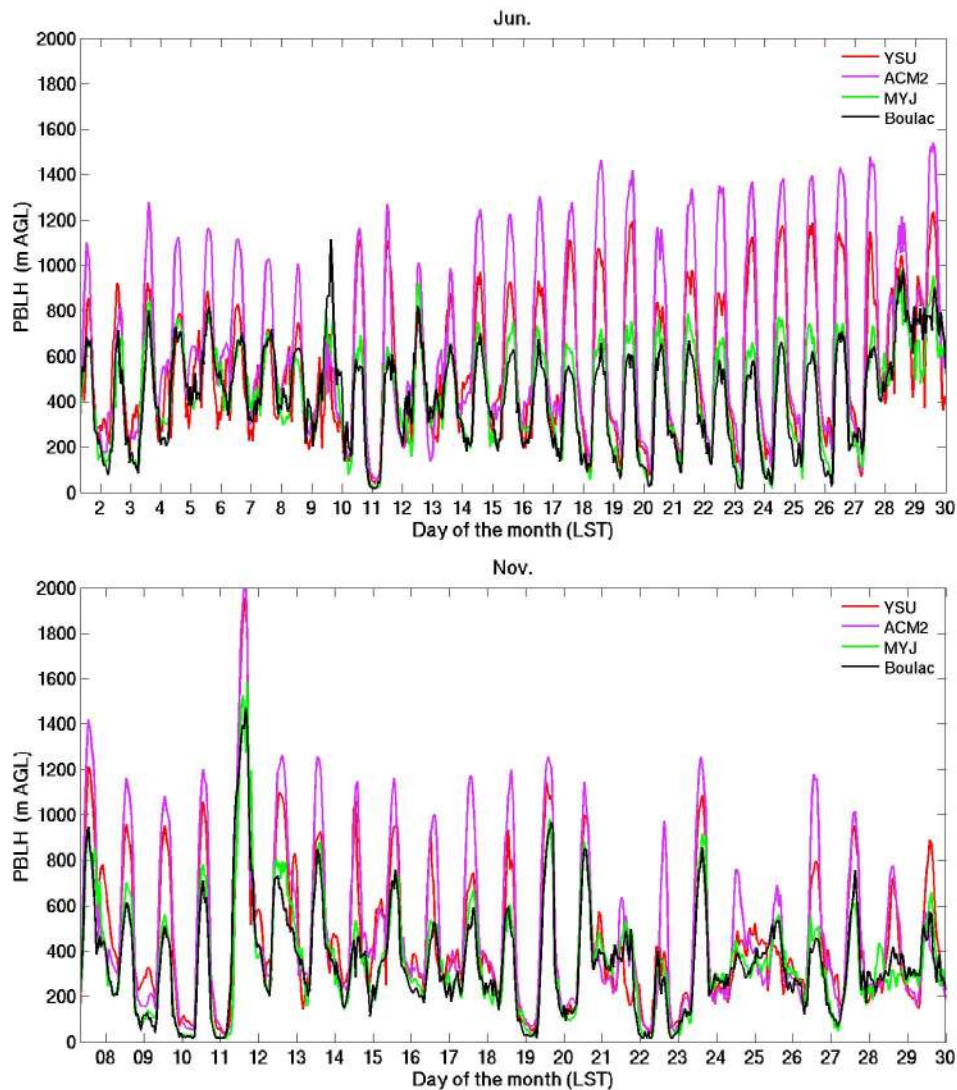
Figure 28. Mean time series of PBL height over 23 sites in Jun and Nov 2006.

differences in PBL height estimation, we superpose model PBL heights over lidar backscattering signals collected at the Yuen Long station. The height at which lidar backscattering signal weakens rapidly as a function of particles and turbulence indicates cessation of rigorous mixing, hence the approximate PBL top [*Menut et al.*, 1999]. Figure 29 shows that both YSU and ACM2 diagnosed PBL heights that fit well with the roll-off band. The PBL heights diagnosed by local PBL schemes are discernibly shallower. This result implies that in local PBL schemes, the prognostic TKE values may be decreasing with height too rapidly or the critical TKE value may not be correct to accurately define the top of PBL. The assumption that fluxes depend solely on local gradients of basic variables is less valid in the CBL. The simulated turbulent mixing should take into account nonlocal contributions when large eddies exist in the lower convective layer and transport fluxes over long distances.

[73] To analyze the diagnosed PBL heights without diagnosis dependencies, we use a unified approach defined in ACM2 algorithm to compute the mixed layer depth. Monin-Obukhov length L, the aforementioned turbulent velocity

scale w_m and dimensionless wind profile function Φ_m in equation 21 are defined as follows:

$$L = \frac{T_o u_*^2}{g k \theta_*} \quad (23)$$

$$w_m = \frac{u_*}{\Phi_m} \quad (24)$$

$$\Phi_m = \left(1 - 16\frac{0.1h}{L}\right)^{-1/4} \quad (25)$$

[74] Where T_o represents the average temperature in the surface layer, θ_* is the surface temperature scale defined as the surface kinematic heat flux divided by friction velocity u_*, and k is the von Karman constant (0.4) [*Monin and Obukhov*, 1954; *Holtslag et al.*, 1990; *Pleim*, 2007a]. The mixed layer depths are then computed with equation (21) and equations (23)–(25) under convective conditions when
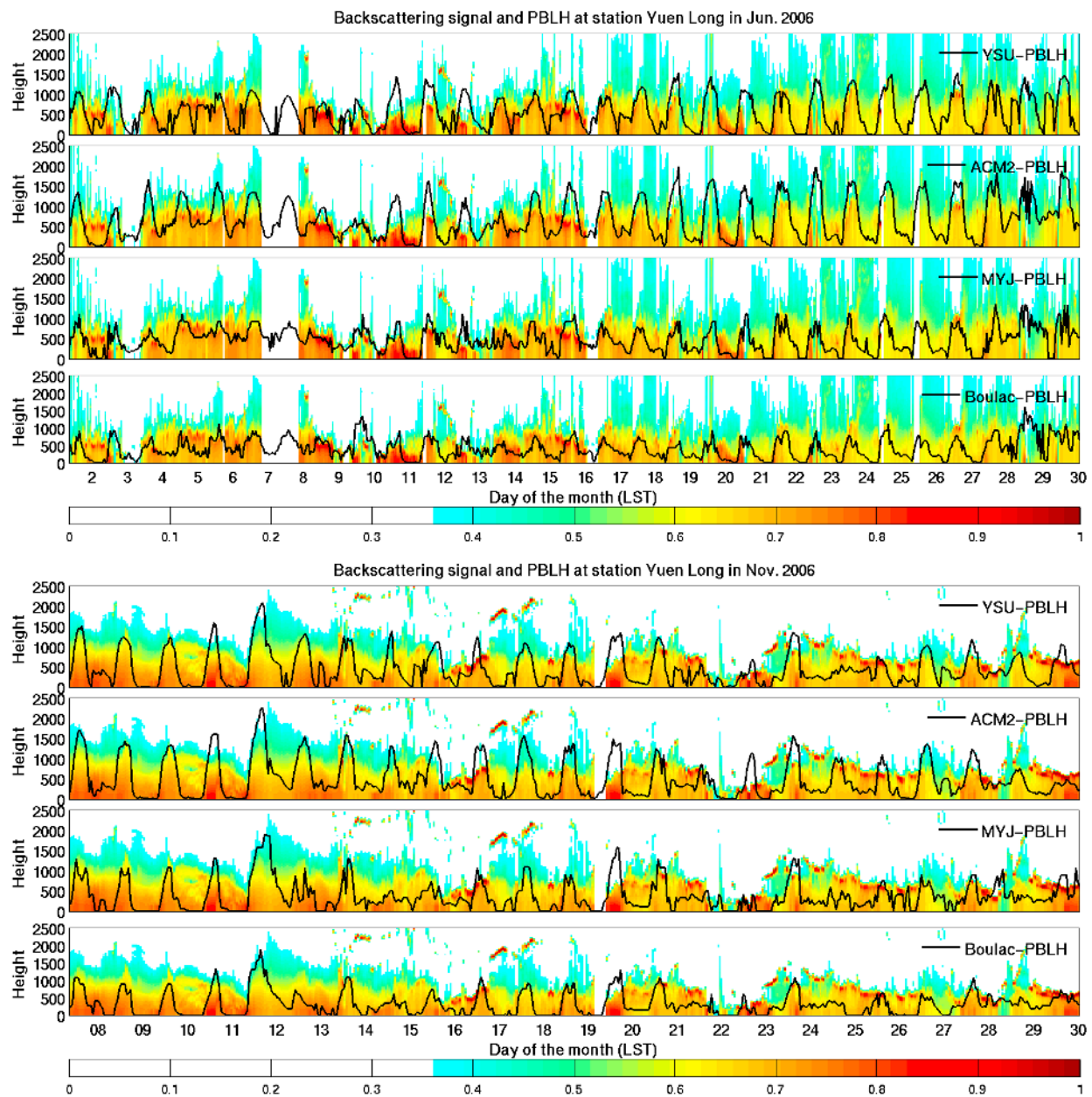
Figure 29. PBL Heights diagnosed by YSU, ACM2, MYJ, Boulac and lidar backscattering signals at Yuen Long station (note that 9th–12th, June and 21st–22nd, November are rainy days).

L is below zero. As shown in Figure 30, the unified diagnosis produces PBL heights with reduced variance among the PBL schemes. This alludes to significant skill difference between local and nonlocal PBL height diagnostic equations. ACM2's mixed layer depth is, as expected, slightly lower than its diagnosed PBL height. However, the fact that YSU's mixed layer depth is slightly greater than its diagnosed PBL height implies that YSU's diagnostic formulation for convective conditions can be improved. In particular, MYJ and Boulac estimate mixed layer depths that are much greater than their diagnosed PBL heights. This leads to the observation that PBL height diagnoses in local PBL schemes generally underestimate.

[75] Both ACM2 and YSU employ PBL height diagnoses based on bulk Richardson number. However, the diagnoses are different in critical value and the definition of lower boundary of the bulk layer. For unstable conditions, ACM2 calculates the bulk Richardson number only above the entrainment layer. There can be another possible reason for the higher diagnosed PBL heights of ACM2 than YSU. From the highly positive correlation between difference in 2 m temperature and difference in PBL height, as shown in Figure 31, we can hypothesize that in ACM2 scenario, where more intense incoming radiation is predicted (discussed in section 4.2.1.2), atmospheric heating is enhanced by thermal plume rise from the surface. This leads to a more
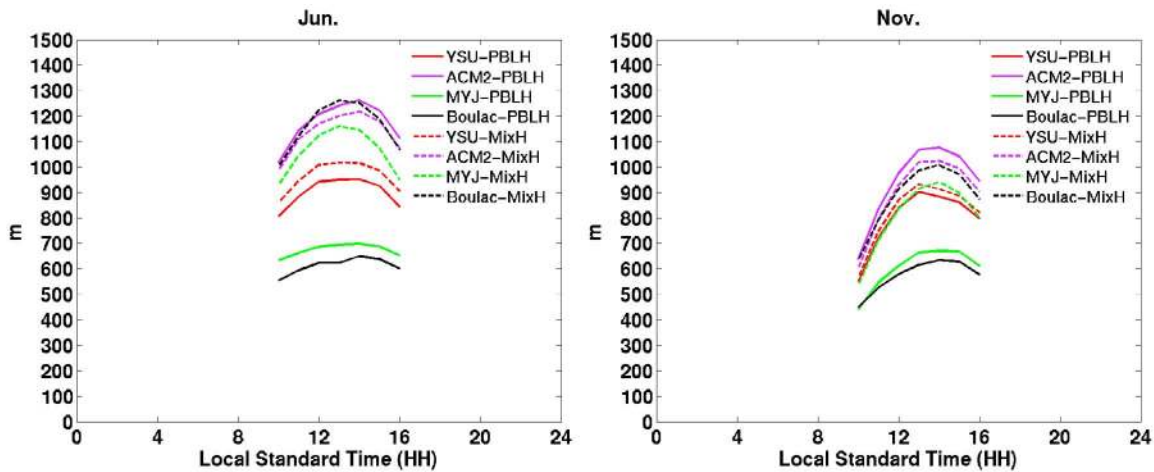
Figure 30. Diurnal mean time series of diagnosed PBL heights and mixed layer heights computed by a unified approach in (left) June and (right) November.

convective mixed layer, and ultimately a deeper planetary boundary layer.

5. Conclusions

5.1. Meteorological Performances at the Surface

[76] The determining driving force for 2 m temperature and heat fluxes is incoming radiation, which, in turn, is influenced by cloud cover (attenuated in the daytime but intensified in the nighttime). The structural evolution of the simulated cloud field is strongly coupled to the subgrid-scale temperature, moisture, and momentum fluxes generated in the PBL scheme. The predicted cloud fraction then affects incoming radiation at the surface, and further results in discrepancy in 2 m temperature estimates through intricate heat exchange processes. Moreover, proper parameterizations in
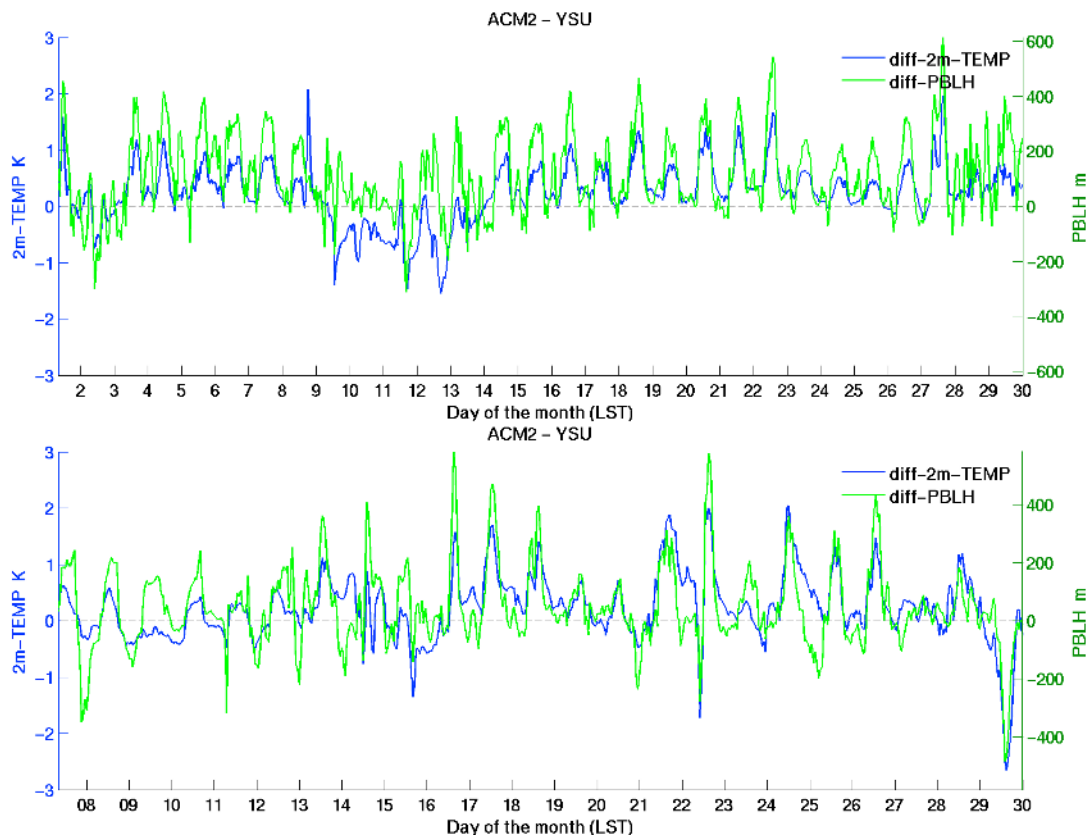
Figure 31. Mean time series of difference (ACM2-YSU) in 2 m temperature (blue line) and difference (ACM2-YSU) in PBL height (green line) over 23 stations: (top) Jun and (bottom) Nov.

the surface layer formulations, particularly the exchange coefficients, are needed to address the uncertainties in reproducing heat fluxes. Overall, nonlocal PBL schemes perform better than local PBL schemes in simulating 2 m temperature and 10 m wind speed. ACM2 correlates best with observation.

5.1.1. The 2 m Temperature Summary

[77] 1. ACM2 produces the best estimation of 2 m temperature as compared with observations in the Hong Kong region over both simulation periods, June and November.

[78] 2. WRF generally underestimates 2 m temperature in the nighttime irrespective of PBL schemes. Overall, ACM2 exhibits the smallest cold bias and MYJ exhibits the largest cold bias during the two months.

[79] 3. The Eta-similarity surface layer scheme predicts a warmer 2 m temperature in the daytime and a colder 2 m temperature in the nighttime than MM5-similarity surface layer scheme. The difference is a manifestation of variations in heat exchange coefficients estimated by the different surface layer formulations.

[80] 4. During certain simulation periods (i.e., June 3rd, 4th, 24th, November 14th, 24th and 28th, when no precipitation had been recorded or simulated), predicted 2 m temperature can be significantly sensitive to the selection of PBL schemes.

5.1.2. The 10 m Wind Speed Summary

[81] 1. Overall, ACM2 gives the best prediction in comparison with 10 m wind speed measurements. Nonlocal PBL schemes lead to more realistic 10 m wind predictions than do local PBL schemes. This assessment holds true in diurnal phase lag, in magnitude, and in performance statistics.

[82] 2. All PBL schemes over-predict wind speed with respect to measurements. Local schemes (MYJ and Boulac) over-predict 10 m wind speed more severely and yield larger positive biases than nonlocal schemes.

5.2. Vertical Profiles Summary

[83] Vertical profiles of horizontal velocity, potential temperature, and water vapor mixing ratio can exhibit significant variances among the PBL schemes across the entire PBL depth. Based on the spatially averaged profiles, nonlocal PBL schemes YSU and ACM2 are often comparable only in form but not in magnitude, likewise for the local PBL schemes MYJ and Boulac (except nocturnal wind profiles). The horizontal velocity and Qv predicted by the four PBL schemes exhibit less difference near the surface. Besides, the choice of surface layer schemes can lead to considerable wind profile differences.

5.2.1. Horizontal Velocity

[84] 1. At 2 A.M. (nighttime), Boulac frequently shows a wind profile shape that is distinct from the other three PBL schemes. This profile shows the slowest wind speed (up to 3 m/s slower than others) below 600 m AGL. However, YSU, ACM2 and MYJ exhibit similar profile shapes at this hour.

[85] 2. At 2 P.M. (daytime), YSU and ACM2 predict near surface wind gradients that are larger than those of local PBL schemes. The nonlocal PBL schemes profiles are nearly constant (convective) within 500 m AGL. ACM2's wind speed is generally lower than YSU within 500 m AGL. MYJ's profile maxima always become the strongest among

certain upper layers (500 m–1200 m AGL over land, 200 m– 600 m AGL over ocean).

[86] 3. The velocity profiles produced by all PBL schemes diff between land and ocean points, but are similar between urban and rural points.

5.2.2. Potential Temperature

[87] 1. In November, YSU and ACM2 always produce warmer temperatures (approximately 1 K on average) than that of local PBL schemes (MYJ and Boulac) below 1000 m AGL over land and ocean at both 2 P.M. and 2 A.M.

[88] 2. The MYJ near surface mean potential temperature is always the lowest among the four PBL schemes at 2 P.M. and 2 A.M. in both two months.

5.2.3. Per-Layer Bulk Richardson Number

[89] 1. At 2 P.M., the per-layer bulk Richardson number profiles of nonlocal PBL schemes are more well-mixed than the local PBL schemes. ACM2 is always the most turbulent in the upper layers where MYJ is always the least turbulent.

[90] 2. At 2 A.M., the differences in per-layer bulk Richardson number profiles are small over land. Over ocean, nonlocal PBL schemes are obviously more turbulent in the upper layers.

5.2.4. Water Vapor Mixing Ratio

[91] 1. Between 400 m and 1200 m AGL, Qvs estimated by the nonlocal PBL schemes are higher than that of the local PBL schemes at 2 P.M. and 2 A.M.

5.3. PBL Heights Summary

[92] Local PBL schemes diagnosed PBL heights that may be too shallow to be realistic.

[93] 1. Both the lidar backscattering signals and the unified approach show that the PBL heights diagnosed by MYJ and Boulac are too shallow. The mixed layer heights computed by the unified approach in different PBL runs are close to each other, which indicate that the discrepancies in diagnosed PBL heights may mostly stem from the disparate definitions in PBL schemes.

[94] 2. Probable causes for ACM2 to diagnose a deeper PBL than YSU are (1) the uncertainties in defining critical bulk Richardson number, (2) the difference in vertical span over which the bulk Richardson number is considered under unstable regimes, and (3) the warmer air temperature simulated by ACM2 PBL which may be favorable for PBL growth and contribute to a thicker planetary boundary layer than that in the YSU. In terms of model physics, the ACM2 approach to limit bulk Richardson number calculation under convective conditions to span only the entrainment layer is superior to YSU's approach.

[95] The choice of PBL schemes has been shown to result in sizable vertical profile differences. Also subject to choice of PBL scheme is variability in near-surface meteorological fields. In relation to K-theory, vertical gradient differences can evolve into variations in diffusion coefficient, or, variations in the intensity of vertical mixing. In air quality modeling context, variation in vertical mixing intensity directly impacts pollutant dispersion characteristics. Likewise, wind profile differences amount to variation in pollutant advection. Preliminary experiments of CAMx simulations and Process Analysis demonstrate that variability in atmospheric chemistry, diffusion, advection and deposition are highly dependent on the PBL structures, hence the choice of PBL schemes. Therefore, a realistic

reproduction of the PBL structure by a mesoscale model is crucial to the accuracy of subsequent air quality modeling and assessment. This study shows that ACM2 is a suitable PBL scheme in WRF for air quality applications in the Hong Kong geographic region.

References

Berg, L. K., and S. Zhong (2005), Sensitivity of MM5-simulated boundary layer characteristics to turbulence parameterizations, *J. Appl. Meteorol.*, *44*, 1467–1483, doi:10.1175/JAM2292.1.

Blackadar, A. K. (1976), Modeling the nocturnal boundary layer, paper presented at Third Symposium on Atmospheric Turbulence, Diffusion and Air Quality, Am. Meteorol. Soc., Raleigh, N. C.

Blackadar, A. K. (1979), High resolution models of the planetary boundary layer, in *Advances in Environmental Science and Engineering*, vol. 1, edited by J. Pfafflin and E. Ziegler, pp. 50–85, Gordon and Breach, N. Y.

Bougeault, P., and P. Lacarrére (1989), Parameterization of orography-induced turbulence in a mesobeta-scale model, *Mon. Weather Rev.*, *117*, 1872–1890, doi:10.1175/1520-0493(1989)117<1872:POOITI>2.0.CO;2.

Burk, S. D., and W. T. Thompson (1989), A vertically nested regional numerical weather prediction model with second-order closure physics, *Mon. Weather Rev.*, *117*, 2305–2324, doi:10.1175/1520-0493(1989)117<2305:AVNRNW>2.0.CO;2.

Chan, A. (2011), Phenomenological significance of urban morphometry in regional atmospheric boundary-layer dynamics, PhD thesis, Hong Kong Univ. of Sci. and Technol., Hong Kong.

Chen, F., and J. Dudhia (2001), Coupling an advanced land surface-hydrology model with the Penn State–NCAR MM5 modeling system. Part I: Model implementation and sensitivity, *Mon. Weather Rev.*, *129*, 569–585, doi:10.1175/1520-0493(2001)129<0569:CAALSH>2.0.CO;2.

Dabberdt, W. F., et al. (2004), Meteorological research needs for improved air quality forecasting: Report of the 11th Prospectus Development Team of the U.S. Weather Research Program, *Bull. Am. Meteorol. Soc.*, *85*, 563–586, doi:10.1175/BAMS-85-4-563.

Deardorff, J. W. (1972), Theoretical expression for the countergradient vertical heat-flux, *J. Geophys. Res.*, *77*, 5900–5904, doi:10.1029/JC077i030p05900.

Han, Z., et al. (2008), Model intercomparison and evaluation of ozone and relevant species—MICS-Asia II, *Atmos. Environ.*, *42*, 3491–3509, doi:10.1016/j.atmosenv.2007.07.031.

Holtslag, A. A. M., and B. A. Boville (1993), Local versus nonlocal boundary-layer diffusion in a global climate model, *J. Clim.*, *6*, 1825–1842, doi:10.1175/1520-0442(1993)006<1825:LVNBLD>2.0.CO;2.

Holtslag, A. A. M., E. I. F. de Bruijn, and H. L. Pan (1990), A high-resolution air mass transformation model for short range weather forecasting, *Mon. Weather Rev.*, *118*, 1561–1575, doi:10.1175/1520-0493(1990)118<1561:AHRAMT>2.0.CO;2.

Hong, S. Y. (2010), A new stable boundary-layer mixing scheme and its impact on the simulated East Asian summer monsoon, *Q. J. R. Meteorol. Soc.*, *136*, 1481–1496, doi:10.1002/qj.665.

Hong, S. Y., and H. L. Pan (1996), Nonlocal boundary layer vertical diffusion in a medium-range forecast model, *Mon. Weather Rev.*, *124*, 2322–2339, doi:10.1175/1520-0493(1996)124<2322:NBLVDI>2.0.CO;2.

Hong, S. Y., Y. Noh, and J. Dudhia (2006), A new vertical diffusion package with an explicit treatment of entrainment processes, *Mon. Weather Rev.*, *134*, 2318–2341, doi:10.1175/MWR3199.1.

Hu, X. M., J. W. Nielsen-Gammon, and F. Zhang (2010), Evaluation of three planetary boundary layer schemes in the WRF model, *J. Appl. Meteorol. Climatol.*, *49*(9), 1831–1844, doi:10.1175/2010JAMC2432.1.

Janjić, Z. I. (1990), The step-mountain coordinate: Physical package, *Mon. Weather Rev.*, *118*, 1429–1443, doi:10.1175/1520-0493(1990)118<1429:TSMCPP>2.0.CO;2.

Janjić, Z. I. (1994), The step-mountain Eta coordinate model: Further development of the convection, viscous sublayer and turbulent closure schemes, *Mon. Weather Rev.*, *122*, 927–945, doi:10.1175/1520-0493(1994)122<0927:TSMECM>2.0.CO;2.

Janjić, Z. I. (1996), The surface layer in the NCEP Eta Model, paper presented at Eleventh Conference on Numerical Weather Prediction, Am. Meteorol. Soc., Norfolk, Va.

Janjić, Z. I. (2002), Nonsingular Implementation of the Mellor-Yamada Level 2.5 Scheme in the NCEP Meso model, *NCEP Off. Note 437*, 61 pp., NCEP, Camp Springs, Md.

Kwok, R. H. F., J. C. H. Fung, A. K. H. Lau, and J. S. Fu (2010), Numerical study on seasonal variations of gaseous pollutants and particulate matters in Hong Kong and Pearl River Delta Region, *J. Geophys. Res.*, *115*, D16308, doi:10.1029/2009JD012809.

Mahrt, L., and M. Ek (1984), The influence of atmospheric stability on potential evaporation, *J. Clim. Appl. Meteorol.*, *23*, 222–234, doi:10.1175/1520-0450(1984)023<0222:TIOASO>2.0.CO;2.

Mellor, G. L., and T. Yamada (1974), A hierarchy of turbulence closure models for planetary boundary layers, *J. Atmos. Sci.*, *31*, 1791–1806, doi:10.1175/1520-0469(1974)031<1791:AHOTCM>2.0.CO;2.

Mellor, G. L., and T. Yamada (1982), Development of a turbulence closure model for geophysical fluid problems, *Rev. Geophys.*, *20*, 851–875, doi:10.1029/RG020i004p00851.

Menut, L., C. Flamant, J. Pelon, and P. H. Flamant (1999), Urban boundary-layer height determination from lidar measurements over the Paris area, *Appl. Opt.*, *38*, 945–954, doi:10.1364/AO.38.000945.

Monin, A. S., and A. M. Obukhov (1954), Basic laws of turbulent mixing in the surface layer of the atmosphere, *Trans. Akad. Nauk SSSR Geofiz. Inst.*, *24*, 163–187.

Noh, Y., W. G. Cheon, S. Y. Hong, and S. Raasch (2003), Improvement of the K-profile model for the planetary boundary layer based on large-eddy simulation data, *Boundary Layer Meteorol.*, *107*, 401–427, doi:10.1023/A:1022146015946.

Pleim, J. E. (2007a), A combined local and nonlocal closure model for the atmospheric boundary layer. Part I: Model description and testing, *J. Appl. Meteorol. Climatol.*, *46*, 1383–1395, doi:10.1175/JAM2539.1.

Pleim, J. E. (2007b), A combined local and nonlocal closure model for the atmospheric boundary layer. Part II: Application and evaluation in a mesoscale meteorological model, *J. Appl. Meteorol. Climatol.*, *46*, 1396–1409, doi:10.1175/JAM2534.1.

Pleim, J. E., and J. S. Chang (1992), A non-local closure model for vertical mixing in the convective boundary layer, *Atmos. Environ., Part A*, *26*, 965–981.

Seaman, N. L. (2000), Meteorological modeling for air-quality assessments, *Atmos. Environ.*, *34*(12–14), 2231–2259, doi:10.1016/S1352-2310(99)00466-5.

Shin, H. H., and S. Y. Hong (2011), Intercomparison of planetary boundary-layer parameterizations in the WRF model for a single day from CASES-99, *Boundary Layer Meteorol.*, *139*, 261–281, doi:10.1007/s10546-010-9583-z.

Skamarock, W. C., et al. (2008), A description of the advanced research WRF version 3, *NCAR Tech. Note TN-475+STR*, 113 pp., NCAR, Boulder, Colo.

Stauffer, D. R., and N. L. Seaman (1990), Use of four-dimensional data assimilation in a limited area mesoscale model. Part I: Experiments with synoptic-scale data, *Mon. Weather Rev.*, *118*, 1250–1277, doi:10.1175/1520-0493(1990)118<1250:UOFDDA>2.0.CO;2.

Stauffer, D. R., and N. L. Seaman (1994), Multiscale four-dimensional data assimilation, *J. Appl. Meteorol.*, *33*, 416–434, doi:10.1175/1520-0450(1994)033<0416:MFDDA>2.0.CO;2.

Stull, R. B. (1984), Transilient turbulence theory. Part I: The concept of eddy-mixing across finite distances, *J. Atmos. Sci.*, *41*, 3351–3367, doi:10.1175/1520-0469(1984)041<3351:TTTPIT>2.0.CO;2.

Stull, R. B. (1988), *An Introduction to Boundary Layer Meteorology*, 666 pp., Kluwer Acad., Dordrecht, Netherlands.

Troen, I., and L. Mahrt (1986), A simple model of the atmospheric boundary layer: Sensitivity to surface evaporation, *Boundary Layer Meteorol.*, *37*, 129–148, doi:10.1007/BF00122760.

Zhang, D. L., and R. A. Anthes (1982), A high-resolution model of the planetary boundary layer—Sensitivity tests and comparisons with SESAME-79 data, *J. Appl. Meteorol.*, *21*, 1594–1609, doi:10.1175/1520-0450(1982)021<1594:AHRMOT>2.0.CO;2.

Zhang, D. L., and W. Z. Zheng (2004), Diurnal cycles of surface winds and temperatures as simulated by five boundary layer parameterizations, *J. Appl. Meteorol.*, *43*, 157–169, doi:10.1175/1520-0450(2004)043<0157:DCOSWA>2.0.CO;2.